





Publication Year	2019
Acceptance in OA @INAF	2021-01-27T16:26:32Z
Title	The Parallelism between Galaxy Clusters and Early-type Galaxies. I. The Light and Mass Profiles
Authors	D'ONOFRIO, MAURO; Sciarratta, Mauro; Cariddi, Stefano; MARZIANI, Paola; Chiosi, Cesare
DOI	10.3847/1538-4357/ab1134
Handle	http://hdl.handle.net/20.500.12386/30054
Journal	THE ASTROPHYSICAL JOURNAL
Number	875



The Parallelism between Galaxy Clusters and Early-type Galaxies. I. The Light and Mass Profiles

Mauro D’Onofrio¹ , Mauro Sciaratta¹ , Stefano Cariddi¹ , Paola Marziani² , and Cesare Chiosi¹ 

¹Department of Physics and Astronomy, University of Padova, Vicolo Osservatorio 3, I-35122, Italy; mauro.donofrio@unipd.it

²INAF—Astronomical Observatory of Padova, Vicolo Osservatorio 5, I-35122, Italy

Received 2018 December 5; revised 2019 March 8; accepted 2019 March 18; published 2019 April 22

Abstract

We have analyzed the parallelism between the properties of galaxy clusters and early-type galaxies (ETGs) by looking at the similarity between their light profiles. We find that the equivalent luminosity profiles of all these systems in the V band, once normalized to the effective radius R_e and shifted in surface brightness, can be fitted by the Sérsic law $r^{1/n}$ and superposed with a small scatter (≤ 0.3 mag). By grouping objects in different classes of luminosity, the average profile of each class slightly deviates from the other only in the inner and outer regions (outside $0.1 \leq r/R_e \leq 3$), but the range of values of n remains ample for the members of each class, indicating that objects with similar luminosity have quite different shapes. The “Illustris” simulation reproduces the luminosity profiles of ETGs quite well, with the exception of in the inner and outer regions, where feedback from supernovae, active galactic nuclei, and wet and dry mergers is at work. The total mass and luminosity of galaxy clusters, as well as their light profiles, are not well reproduced. By exploiting simulations, we have followed the variation of the effective half-light and half-mass radius of ETGs up to $z = 0.8$, noting that progenitors are not necessarily smaller in size than current objects. We have also analyzed the projected dark+baryonic and dark-only mass profiles, discovering that, after a normalization to the half-mass radius, they can be well superposed and fitted by the Sérsic law.

Key words: galaxies: clusters: general – galaxies: evolution – galaxies: photometry – galaxies: structure

1. Introduction

Recently, Cariddi et al. (2018) derived the equivalent luminosity profiles in the V and B bands of several nearby galaxy clusters observed by the surveys WINGS and Omega-WINGS (Fasano et al. 2006; Varela et al. 2009; D’Onofrio et al. 2014; Moretti et al. 2014b; Gullieuszik et al. 2015). In these light profiles, the average surface brightness is measured on circles of increasing radius centered on the position of the brightest cluster galaxy. Their work showed that galaxy clusters share many properties in common with early-type galaxies (ETGs): the behavior of the growth curves and surface brightness profiles, the distribution in the Kormendy and Faber–Jackson relations (Faber & Jackson 1976; Kormendy 1977), and the existence of a similar color–magnitude diagram. They further showed that galaxy clusters are best fitted by the Sérsic $r^{1/n}$ law (Sérsic 1968) and might be nonhomologous systems like ETGs (Caon et al. 1993; D’Onofrio et al. 1994).

These striking parallelisms between systems so different in size are particularly interesting when the mechanisms of structure assembly are considered in the current cosmological framework. These parallelisms are not unknown: previous works already noted some interesting similarity between clusters and ETGs. The best-known example is the observed distribution of clusters in the fundamental plane (FP) relation³ (Djorgovski & Davis 1987; Dressler et al. 1987). Schaeffer et al. (1993), Adami et al. (1998), and D’Onofrio et al. (2011) showed that galaxy clusters share approximately the same FP relation of ETGs. This is not surprising if we think that clusters are almost virialized structures with a similar dynamics. The FP relation is, in fact, a universal relation for several gravitating systems closed to the virial equilibrium, such as globular clusters (see, e.g., Djorgovski 1995; McLaughlin 2000; Barmby et al. 2007),

cluster spheroids (Zaritsky et al. 2006), open clusters (Bonatto & Bica 2005), X-ray-emitting elliptical galaxies (Diehl & Statler 2005), clusters of galaxies (see, e.g., Lanzoni et al. 2004), supermassive black holes (SMBHs; e.g., Hopkins et al. 2007), and quasars (e.g., Hamilton et al. 2006). Its tilt with respect to the prediction of the virial theorem has several possible origins.

Another example comes from the luminosity profiles. The ETGs and clusters are best fitted by the Sérsic $r^{1/n}$ law (see, e.g., Caon et al. 1993; Cariddi et al. 2018), and it is well known that the index n correlates with many observable parameters, such as luminosity M_V , effective radius R_e , and effective surface brightness $\langle \mu \rangle_e$ (Caon et al. 1993; Graham & Guzmán 2003). The systematic variation of n in ETGs is interpreted as a deviation from structural and dynamical homology in collisionless stellar systems (Ciotti 1991; Ciotti & Bertin 1999; Graham 2001, 2002; Graham et al. 2003; Trujillo et al. 2004). The final value of n probably results from several dissipationless merging events. The nearly exponential value of n (~ 1) observed in dwarf systems is similar to that of disk objects, suggesting that gas collapsed and dissipated energy, while the large value of n in luminous ETGs is due to merging, with wet events in the remote epochs and dry events in the recent ones. This scenario seems to be supported by numerical simulations (see, e.g., Scannapieco & Tissera 2003; Eliche-Moral et al. 2006). If clusters are indeed nonhomologous systems like ETGs, what produces the observed variations of n ? Why do clusters share the same properties of ETGs when we look at their luminosity profiles?

Cariddi et al. (2018) further showed that in the $M_V - (B - V)$ plane, galaxy clusters share the same “red-sequence” slope of ETGs, where the mean color is measured within $0.6 R_{200}$.⁴ In other words, small/faint clusters are bluer than

³ The FP is the relation between the effective radius R_e , the effective surface brightness $\langle \mu \rangle_e$, and the central velocity dispersion σ_0 .

⁴ Here R_{200} is the radius at which the projected density is 200 times the critical density of the universe.

big/bright clusters. The same trend is observed in galaxies. Why do we see such a similar color–magnitude diagram?

On the theoretical side, numerical simulations of the cold dark matter (CDM) universe predict that halos are nearly self-similar (see, e.g., Dubinski & Carlberg 1991; Navarro et al. 1996; Moore et al. 1998; Ghigna et al. 2000). The collapsed halos have, in general, a central density cusp with a $\rho \propto r^{-1}$ profile that at large radii becomes $\rho \propto r^{-3}$. These slopes are characteristic of the Navarro–Frenk–White (NFW) profile (Navarro et al. 1996), which provides a good description of N -body simulations. Merritt et al. (2005), however, showed that the Sérsic law might provide equally good fits for the density profiles of dark matter (DM) halos with small central deviations that can be attributed to dynamical effects (van der Marel 1999; Milosavljevic et al. 2002; Ravindranath et al. 2002; Graham 2004; Merritt et al. 2004; Preto et al. 2004). This suggests that a “universal” mass profile might exist for galaxies and clusters and that the observed deviations originate in the complex physics of the luminous baryon component.

Improved simulations at high resolution showed that DM halos are not strictly self-similar (Merritt et al. 2006; Navarro et al. 2010) and can also vary their shape for the action of baryonic matter (BM). Cooling might allow baryons to condense toward the center, producing a higher concentration of DM (e.g., Blumenthal et al. 1986; Gnedin et al. 2004; Pedrosa et al. 2009; Abadi et al. 2010), and heating of the central cusp could be induced by dynamical friction (e.g., El-Zant et al. 2001; Nipoti et al. 2004; Romano-Díaz et al. 2008; Del Popolo & Cardone 2012), feedback from supernovae (Governato et al. 2010, 2012), and feedback from active galactic nuclei (AGNs; Peirani et al. 2008; Martizzi et al. 2012).

Understanding the relative contribution of the dark and luminous components in ETGs and clusters is therefore important. As a matter of fact, if the CDM description of the universe is correct, then the structure of the real halos of such systems can provide much information about the assembly of the structures themselves, indicating what the imprint of baryons on their halos was. The dark and baryonic density profiles and the distribution in the main scaling relations can furthermore inform us about the relative importance of dissipational and dissipationless processes that occurred in the evolution of systems, as well as the relative weight of the feedback processes and assembly of the central SMBHs.

This is the first paper of a series dedicated to the study of clusters and ETGs. The aim is to describe the properties that these systems have in common and test the ability of current hydrodynamical models in reproducing the observational evidence. The paper is designed as follows. In Section 2, we introduce the galaxy sample and the construction of the equivalent surface brightness profiles of galaxies and clusters. In Section 3, we present the results obtained in real galaxies, comparing the light profiles of ETGs and clusters (Section 3.1) and discussing their nonhomology (Section 3.2). In Section 4, we introduce the Illustris data set of hydrodynamical simulations, presenting the light profiles derived for galaxies and clusters (Genel et al. 2014; Vogelsberger et al. 2014; Nelson et al. 2015). In Section 4.1, we check the degree of nonhomology emerging from simulated data; in Section 4.2, we look at the evolution of the effective radius of ETGs up to redshift $z = 0.8$; and in Section 4.3, we analyze the mass profiles of ETGs and clusters coming from the simulated data.

Finally, in Section 5, we summarize our conclusions. In the Appendix, we provide several tables with the data used in this work.

Throughout the paper, we assumed in all of our calculations the same values of the Λ CDM cosmology used by the Illustris simulation (Vogelsberger et al. 2014): $\Omega_m = 0.2726$, $\Omega_\Lambda = 0.7274$, $\Omega_b = 0.0456$, $\sigma_8 = 0.809$, $n_s = 0.963$, and $H_0 = 70.4 \text{ km s}^{-1} \text{ Mpc}^{-1}$.

2. The Sample

The sample of clusters analyzed here is that of the WINGS and Omega-WINGS surveys (Fasano et al. 2006; Varela et al. 2009; D’Onofrio et al. 2014; Moretti et al. 2014b; Gullieuszik et al. 2015). With respect to the original WINGS sample, the number of clusters is limited to 45 objects (those of the southern hemisphere covered by the Omega-WINGS survey with available spectroscopic measurements; Cava et al. 2009; Moretti et al. 2014a). The luminosity profiles of these galaxy clusters were derived by Cariddi et al. (2018) by integrating the luminosity growth curves in the V and B bands. These were obtained by statistically subtracting the contribution of background objects and taking into account all sources of incompleteness. The growth curves were then fitted using the Sérsic law and transformed in surface brightness units. The corresponding cluster structural parameters, half-light radius R_e , and mean surface brightness $\langle I \rangle_e$ were also derived by Cariddi et al. (2018) by integrating the circular luminosity growth curves of clusters.

The ETGs studied here for the comparison with galaxy clusters are the brightest (BCG) and second-brightest (II-BCG) cluster galaxies plus a sample of normal ETG members of the clusters (one for each cluster) randomly chosen in the CCD images. The main structural parameters of these galaxies were already derived by D’Onofrio et al. (2014) through the software GASPHOT (Pignatelli et al. 2006). However, for these objects, we have rederived the equivalent surface brightness profiles in a completely independent way using the software AIAP (Fasano et al. 2010). The reason for this reanalysis is that we want to compare the light profiles of galaxies and clusters in a rigorous way up to the faintest level in surface brightness. Figure 1 shows an example of the accuracy reached by both methods of analysis. The GASPHOT and AIAP profiles are compared for four objects taken randomly from the sample. Note that the GASPHOT profiles are less deep in surface brightness and less noisy. Some differences among the profiles are present and due to the fact that the two software packages AIAP and GASPHOT work in a different way. The package AIAP performs the photometric analysis of the single galaxies by manually constructing all of the isophotes. All sources of disturbance (stars, background galaxies, stellar spikes, etc.) are previously masked, and the data are smoothed when the sky background does not permit the drawing of a clear isophote. All isophotes are then fitted by ellipses and with the $r^{1/4}$ or $r^{1/n}$ law. On the other hand, GASPHOT is an automatic procedure based on the SExtractor analysis. This software does not permit the accuracy of the manual procedure, in particular when disturbing objects are superposed to the galaxy image. The fainter surface brightness reached by AIAP is a consequence of this different approach.

The typical photometric error in the light profile is $\sim 10\%$ at $\mu(V) \sim 26 \text{ mag arcsec}^{-2}$ (Fasano et al. 2006). The photometric error bars are not shown in the figure. They are, in fact, poorly known for several reasons. (1) The automatic procedure

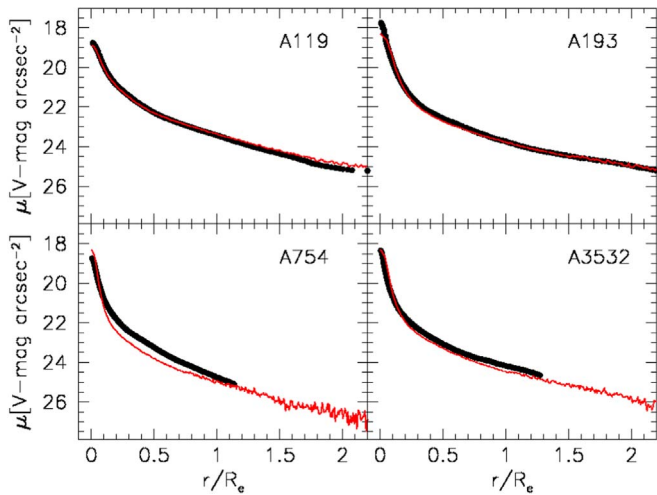


Figure 1. Comparison between the equivalent surface brightness profiles of the BCGs derived with GASPHOT (black lines) and AIAP (red lines). The cluster name is labeled in each box.

performs the fit of the major and minor axis profiles of the galaxies by convolving the $r^{1/n}$ law with an average point-spread function (PSF) derived for the image. It follows that the photometric error close to the central region might be larger than 10%. (2) In the outer region, the effects of the sky subtraction can be substantial. The software subtracts a constant value derived in a region around each galaxy, but in some cases, this is not sufficient to get a high accuracy in the profiles. The sky background might change for the proximity of bright objects. Since an accurate determination of the errors in the profiles would require a more complex analysis, and our aim here is to compare the average profiles of classes of objects, we have not taken into account the errors of the single profiles, but only the standard deviation around the mean of the average profiles.

The Sérsic index n of our objects has also been remeasured by fitting the AIAP growth curve profiles. Figure 2 shows the comparison between the Sérsic indexes measured by GASPHOT and AIAP. We see that there is a substantial agreement, but the typical error Δn is quite large (~ 1). The large uncertainty in the value of n depends on several factors: the interval used for the fit, the FWHM of the seeing, and the correct estimate of the sky background in the surface brightness and growth curve profiles. For these reasons, we decided to set the error Δn to 1 for all of the data, and we have only shown the equality line. The aim of Figure 2 is simply to stress the difficulty of trusting in the values of n when different methods are used to get it. At the end of this reanalysis, we decided to keep the structural parameters of the galaxies derived by GASPHOT, since this software provides a seeing-convolved fit of the major and minor axis surface brightness profiles of each object at the same time, giving in output the Sérsic index n , the effective radius R_e , the effective surface brightness $\langle I \rangle_e$, and the average flattening (b/a) . The AIAP profiles have been used instead in our figures to better show the behavior of the profiles at the faintest level of surface brightness.

3. Results with the Observational Data

Here we start the presentation of the results obtained from our analysis of the observational data.

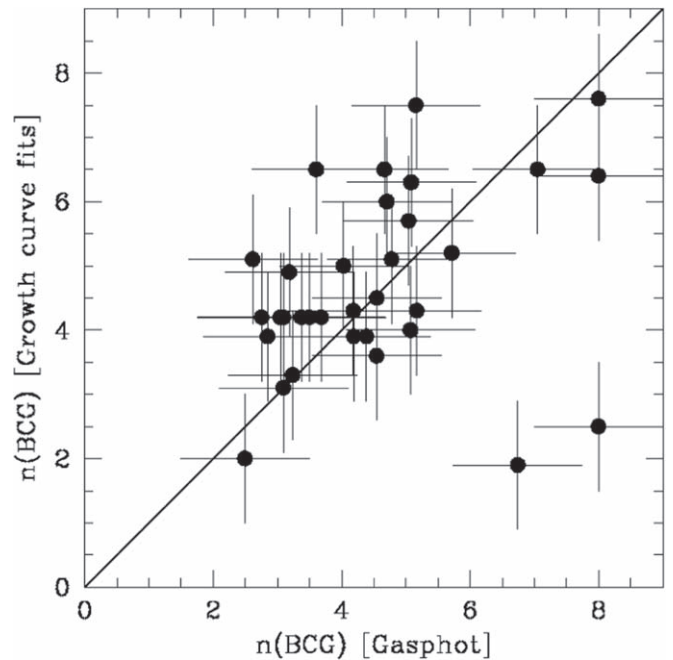


Figure 2. Comparison of the Sérsic indexes of the BCGs derived with GASPHOT and those derived from the fit of the growth curves. The errors on n have been set to 1 for all objects (see text).

3.1. The Light Profiles of the ETGs and Clusters

First we remind readers that the profiles are in the V band and are equivalent profiles, i.e., average surface brightness measured in circles of increasing radius centered on the peak luminosity. All profiles have been normalized to the effective radius: that enclosing half the total luminosity.

What we discuss is not the single profile of each object but rather the average profile for the class of objects defined in the above section (BCGs, II-BCGs, random normal ETGs, and clusters). The average profiles have been derived in two ways: (1) by considering the mean value of the surface brightness for all of the profiles of each class and (2) by shifting all of the profiles with respect to one reference object. In this case, after finding the shift that produces the lowest average residuals in the selected interval, we have derived the mean profile among the whole set of shifted profiles.

We have chosen the BCG, II-BCG, and normal ETG in A160 as a reference for galaxies and the profile of the cluster A160 as reference for clusters. The choice of A160 as a reference does not influence the conclusions we draw below. Any other reference object in different clusters produces the same results. The two methods do not produce significantly different results. The left panel of Figure 3 shows the average profiles obtained for BCGs (black dots), II-BCGs (red dots), and normal ETGs (green dots). Note the small difference in the right panel obtained with the second method. The average profiles indicate that normal ETGs are systematically brighter than BCGs in surface brightness at each r/R_e . The II-BCGs are also a bit brighter than the BCGs. We will see in Section 4 that this behavior is reproduced by numerical simulations.

The average cluster profile, shown in blue in Figure 3, was obtained by excluding the profiles of the following clusters: A85, A147, A151, A168, A1991, A2399, A2415, A2457, A3158, A3528a, A3809, A3128, and A3880. The profiles of these clusters show clear evidence of the presence of more

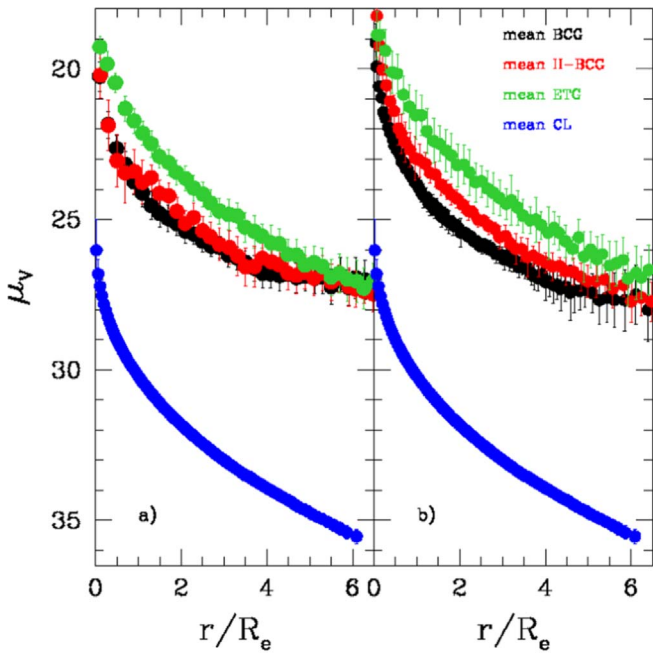


Figure 3. Panel (a): average surface brightness profiles for each class of objects (galaxies and clusters). The average profile of the BCGs is marked by black dots, II-BCGs by red dots, normal ETGs by green dots, and clusters by blue dots. The error bars give the 1σ standard deviation around the mean value. In panel (b), all of the profiles have been previously shifted with respect to the corresponding reference object A160 and then averaged (see text).

complex structures (double components and anomalous behavior of the growth curves) that we believe likely originated from recent merging events that occurred in these clusters. The shape of these profiles indicates that in our sample, $\sim 30\%$ of the clusters have not yet reached a completely relaxed photometric structure (i.e., the profiles cannot be fitted with one single Sérsic component). This is a significant fraction; however, the inclusion of non-Sérsic profiles would not permit a correct comparison with ETGs.

Figure 3 clearly shows that the surface brightness profiles of each class, once normalized to the effective radius, can be superposed with a small scatter (the typical rms is $\sim 0.3 \div 0.5$ mag) once a constant shift in surface brightness is applied. To obtain a superposition of the profiles in surface brightness, depending on the interval chosen to realize the match, one must add one of the values reported in Table 1.

The result of the superposition is better visible in Figure 4, where the profiles of all classes have been shifted by a constant value using the average profile of the BCGs as reference. We have imposed a vertical shift minimizing the difference in μ_V in all bins of r/R_e ; the shift is calculated as

$$s_j = \frac{1}{N} \sum_{i=1}^N \mu_{\text{simBCG}}(r_i/R_e) - \mu_j(r_i/R_e), \quad (1)$$

where N is the number of radial bins in which the difference is evaluated, while j refers to any other kinds of structures except simulated BCGs. All values of s_j are reported in Table 1.

The profiles in Figure 4 are shown in log scale to better put into evidence the differences among them. The figure indicates that all profiles are well superposed (within ~ 0.3 mag) in the interval $0.3 \leq r/R_e \leq 2.5$, while the differences emerge in the center ($r/R_e \leq 0.3$) and outer regions ($2.5 \leq r/R_e \leq 6.3$).

Since the seeing was not exactly the same in each CCD image, the average profile we get is still affected by the seeing

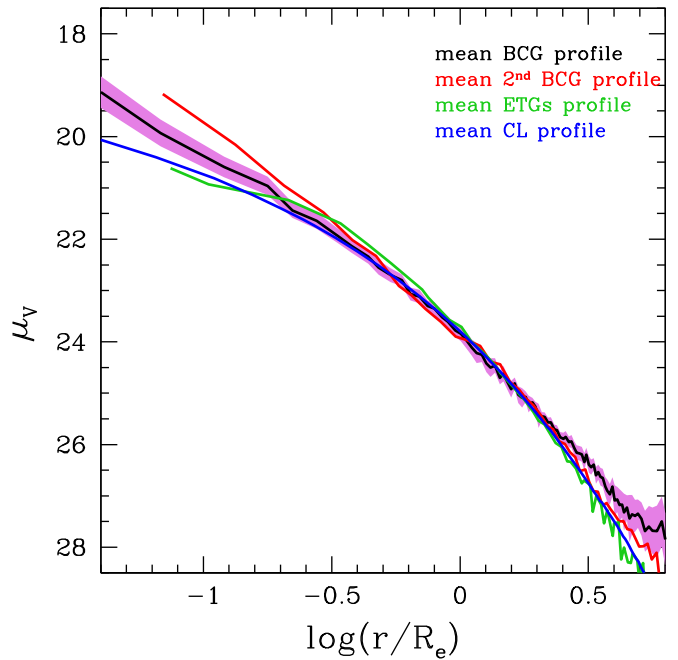


Figure 4. Average surface brightness profiles for each class of objects in log scale. The color code is in the legend. The equivalent surface brightness profiles are shown here superposed with respect to the BCG profile chosen as reference. The shaded area marks the 1σ error in the distribution of the BCG profiles around the reference BCG in A160.

Table 1
Values of the Constant Shift s_j Used to Superpose the Average Surface Brightness Profiles in Figure 3

Obs. Obj.	s_j
BCG	0.0
II-BCG	$0.4 \div 0.8$
ETG	$1.5 \div 2.0$
CL	$-6.5 \div -7.0$

Note. The average profile used as reference is that of BCGs.

in its central part. However, to a first-order approximation, this is not strictly a problem for our analysis, since we are interested in the relative comparison between the profiles of different classes. After averaging the profiles, the same average seeing effect is present in all profiles, so the relative difference can be considered almost free from the effect of seeing. The average cluster profile is not affected by seeing, being simply the sum of the light of the single galaxy members of clusters.

The differences observed in the central region of Figure 4, however, require a more careful analysis of the seeing effects. The seeing effects can be quite different for big and small galaxies. Furthermore, one should also consider that all profiles are rescaled in units of r/R_e , with R_e spanning a big interval of values (see below).

We have therefore repeated the analysis of the profiles using the Sérsic growth curve models obtained by GASPHOT. Once convolved with the PSF, these models give the observed growth curves that, divided by the area, provide the surface brightness profiles. They are, in practice, the deconvolved integrated magnitude profiles of our objects, not affected by the seeing.

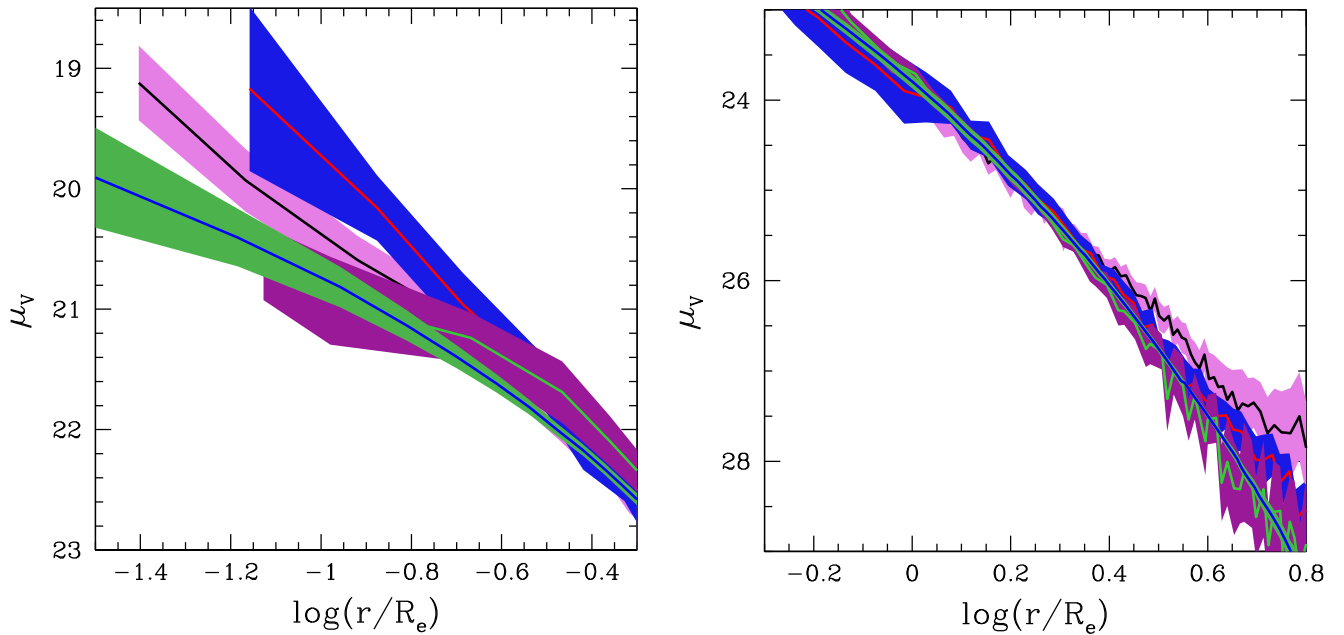


Figure 5. Zoom on the inner (left panel) and outer (right panel) regions of Figure 4. The colored bands mark the 1σ error around the mean profile of each class. As in previous figures, the black line marks BCGs, the red II-BCGs, the green normal ETGs, and the blue clusters. The shaded area in pink is used for BCGs, the blue for II-BCGs, the violet for normal ETGs, and the green for clusters.

Figure 5 shows a zoom of the inner and outer regions of Figure 4. The colored bands mark the 1σ error around the mean profile of each class. We clearly see that in the inner region, the mean profile of BCGs differs from that of II-BCGs and clusters at more than 1σ , while normal ETGs are always consistent with the cluster profile. In the outer region, such differences remain, although they are less marked.

Figure 6 shows the growth curves of our classes of objects shifted artificially to the BCG curve in linear (top panel) and log (bottom panel) scale. Note that in this figure, we have the integrated magnitude within circular apertures and not the surface brightness. The log scale indicates that normal ETGs once superposed to BCGs are in general fainter at each r/R_e , while II-BCGs are brighter than BCGs. This confirms that the seeing effects have not significantly affected the distribution observed in Figure 4.

Figure 7 shows the average profile of BCGs and the fit we get with the Sérsic law. In general, good fits are obtained for all averaged profiles with this empirical law.

The fitted equation is

$$\mu(r) = \mu_e + \frac{2.5b_n}{\ln(10)} \left[\left(\frac{r}{R_e} \right)^{1/n} - 1 \right]. \quad (2)$$

Table 2 gives the Sérsic index n and the value of the term b_n from Equation (2), together with their uncertainty. The last column reports the 1σ scatter around the fit. Note how the value of n for galaxies decreases when the fit is done for objects of small mass. The 1σ error around the fits is in general very low, indicating that the Sérsic law works very well for ETGs and clusters.

The good match between the light profiles of clusters and ETGs and the good fits obtained with the Sérsic law for both classes are the first element of the claimed parallelism.

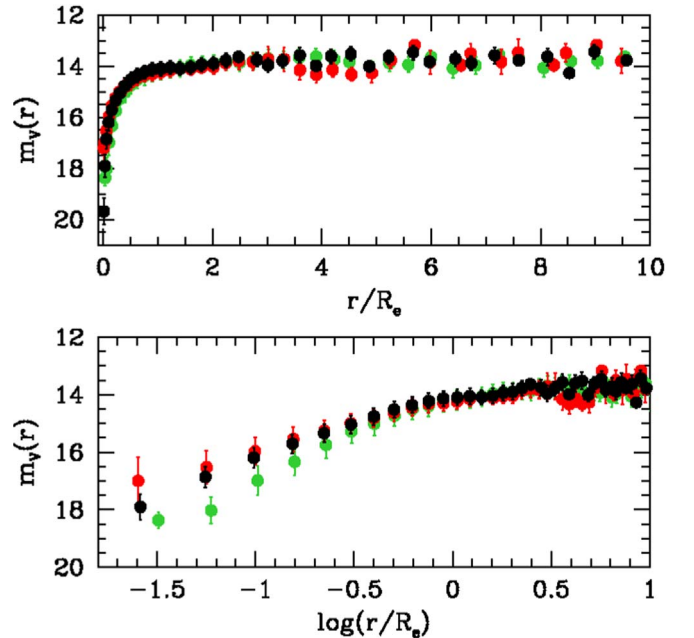


Figure 6. Top panel: average deconvolved growth curve profiles for each class of objects in linear scale. Radii are normalized to the effective radius. As before, BCGs are marked by black dots, II-BCGs by red dots, and normal ETGs by green dots. The error bars give the 1σ standard deviation around the mean profile.

3.2. Nonhomology

The nonhomology of ETGs is well known after Caon et al. (1993), D’Onofrio et al. (1994), and Graham & Colless (1997). They showed that the surface brightness profiles of ETGs are best fitted by the Sérsic law $r^{1/n}$ and that the index n is correlated with the effective radius and total luminosity. This means that the average shape of ETGs depends on the total

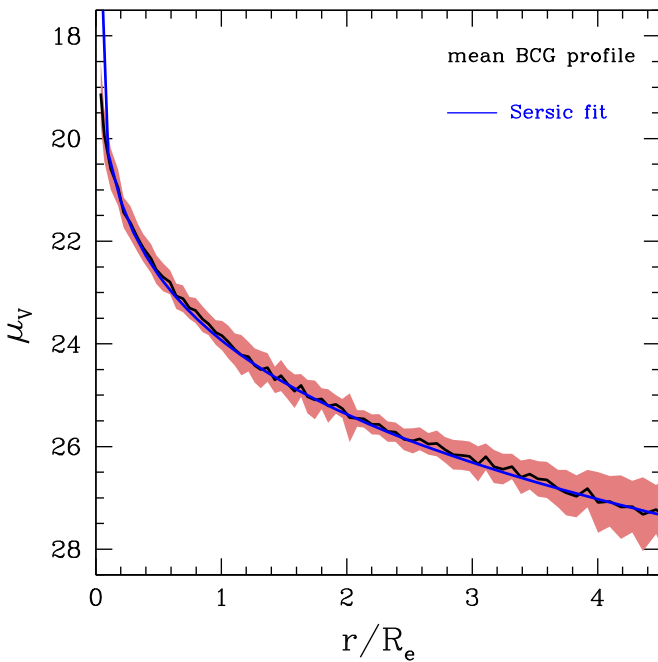


Figure 7. Fit of the average profile of BCGs (black line) with the Sérsic law (blue line).

Table 2

Best Sérsic Fit Parameters for the Average Surface Brightness Profiles of Observed and Simulated Galaxies and Clusters

Obs. Obj. ($z = 0$)	n	Δn	$b(n)$	$\Delta b(n)$	σ
BCGs	5.27	0.28	9.46	0.53	0.08
II-BCGs	4.76	0.39	9.40	0.84	0.11
ETGs	2.78	0.13	5.56	0.30	0.18
CLs	2.58	0.01	4.81	0.02	0.01
Sim. obj. ($z = 0$)	n	Δn	$b(n)$	$\Delta b(n)$	σ
BCGs	6.41	0.31	12.52	0.65	0.05
II-BCGs	4.93	0.15	9.72	0.32	0.05
ETGs	1.77	0.03	3.17	0.08	0.19
CLs	3.15	1.35	5.60	2.50	0.23

Note. The errors related to the parameters and values of the 1σ scatter are reported. The fits have been computed in the range $r/R_e \in [0, 6]$ for real objects and $r/R_e \in [0, 3]$ for simulated objects.

mass (and luminosity) of the systems. Some years ago, ETGs were thought to be perfectly homologous systems, i.e., self-similar structures simply scaled for a constant factor, with luminosity profiles following the de Vaucoulers $r^{1/4}$ law.

The left panel of Figure 8 shows the distribution of our systems in the $\log(R_e) - \log(n)$ plane. The values of n used here are those derived by D’Onofrio et al. (2014) with GASPHOT for the single ETGs and Cariddi et al. (2018) for clusters. Note the solid line, which represents the best fit of the whole distribution of ETGs (BCGs+II-BCGs+random ETGs). This line has been shifted along the y-axis matching the distribution of clusters. We have chosen the shift that minimizes the average difference of the residuals. The fit has been obtained with the standard least square technique using the program SLOPES (Feigelson & Babu 1992), which performs a bootstrap and jackknife resampling of the data without taking into account the measurement errors. We get $\log(R_e) = 2.0 \log(n) + 2.72$ with an rms = 0.42, a correlation coefficient (c.c.) of 0.48, and a Spearman significance of

$2.0 \cdot 10^{-9}$. This means that the correlation exists and is quite robust. Note that, looking at the single families of objects of different colors in the plot, the correlation between the two variables is much less pronounced and even absent for clusters, although the interval of values of n is quite large for each class. The global fit clearly does not represent the trend observed for each class of objects taken separately (see the dashed lines). A smaller slope is obtained for each class: 1.06 (BCGs), 1.57 (II-BCGs), 0.91 (random normal ETGs), and 0.96 (clusters). The rms/c.c. is 0.15/0.38 (BCGs), 0.27/0.55 (II-BCGs), 0.17/0.37 (random normal ETGs), and 0.22/0.12 (clusters). The resampling analysis gives an error on the slopes of 0.2 for the fit of the whole ETG sample, so that in practice, the observed difference with the other slopes is statistically significant.

This behavior is expected because we have defined three categories of objects with well-defined values for the mass and luminosity in a quite restricted interval of values (see the top panel of Figure 11). Observe that in each class, the shape is far from being similar for all objects. The values of n are quite large in each class, so the correlation with R_e almost disappears.

For clusters, the significance of the correlation is small ($4.2 \cdot 10^{-1}$), while it is always better than 10^{-3} for all other systems. The spread of values of n , however, is quite large.

Along the same lines, the right panel of Figure 8 shows the distribution of our systems in the $\log(L) - \log(n)$ space. Here again, the fit is quite good for the whole distribution of ETGs: $\log(L) = 2.31 \log(n) + 9.38$ with an rms = 0.53, a c.c. of 0.42, and a significance of $1.5 \cdot 10^{-7}$. For the single classes of objects, we get for the slope/rms/c.c. $-1.03/0.19/-0.065$ (BCGs), $1.16/0.23/0.32$ (II-BCGs), $1.34/0.25/0.52$ (random normal ETGs), and $-0.09/0.19/-0.19$ (clusters). The error on the slope obtained for the global sample of ETGs is 0.32, so the difference with the other slopes is significant.

As before, the relation of nonhomology can be defined only when a heterogeneous set of ETGs is used. For single classes of objects, the relation is not well defined. In particular, for BCGs and clusters, despite the values of n being quite large ($2 < n < 8$ for BCGs and $0.4 < n < 5$ for clusters), the correlation is absent.

Our clusters have approximately similar luminosity, so they do not show a clear relation between n and R_e or L . The different shapes of the light profiles, however, imply that significantly different structures are possible for clusters and bright galaxies of similar mass. In this respect, we can consider cluster nonhomologous systems as ETGs.

Figure 9 shows the histograms of the distributions of the Sérsic index n for the different classes of objects. Note the spread of values of n in each class and the increased value of n for the brightest galaxies.

In conclusion, we can say that all of our systems are nonhomologous in the sense that at any given mass, they might correspond to quite different shapes.

This is the second clear parallelism.

4. Comparison with Numerical Simulations

Our aim here is to check to what extent current numerical simulations are able to reproduce the observed properties of real galaxies and clusters. We have chosen the data provided by the Illustris simulation⁵ (Genel et al. 2014; Vogelsberger et al. 2014; Nelson et al. 2015, to whom we refer for all details), a suite of large, highly detailed hydrodynamics cosmological

⁵ <http://www.illustris-project.org/data/>

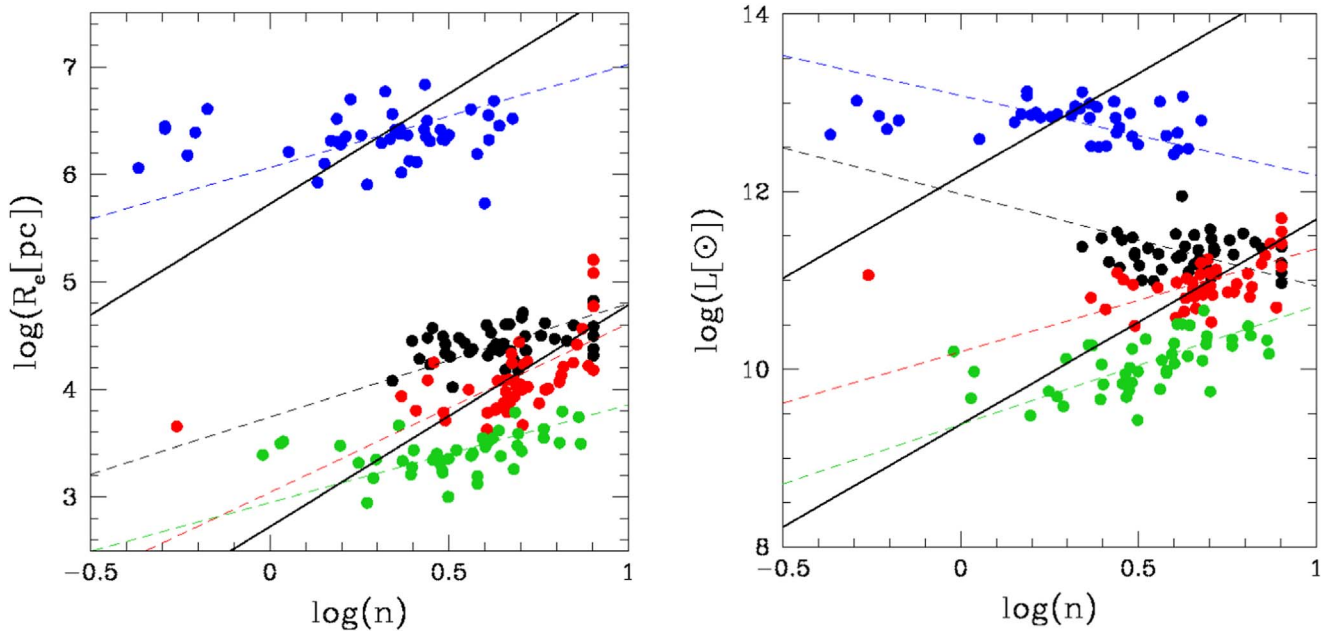


Figure 8. Left panel: distribution of ETGs and clusters in the $\log(R_e)$ – $\log(n)$ plane. Black dots are BCGs, red dots are II-BCGs, green dots are random ETGs, and blue dots are clusters. The lower solid line marks the fit of the whole distribution of ETGs (BCGs+II-BCGs+random normal ETGs). The upper solid line is a shifted version of this fit used to best match the cluster distribution. Right panel: distribution of ETGs and clusters in the $\log(L)$ – $\log(n)$ plane. The symbols are the same as in the left panel. The lower solid line marks the fit of the whole distribution of ETGs (BCGs+II-BCGs+random normal ETGs). The upper solid line is a shifted version of the lower solid line done to best match the cluster distribution. The colored dashed lines are the individual fits obtained by the program SLOPES (see text) for the different classes of objects.

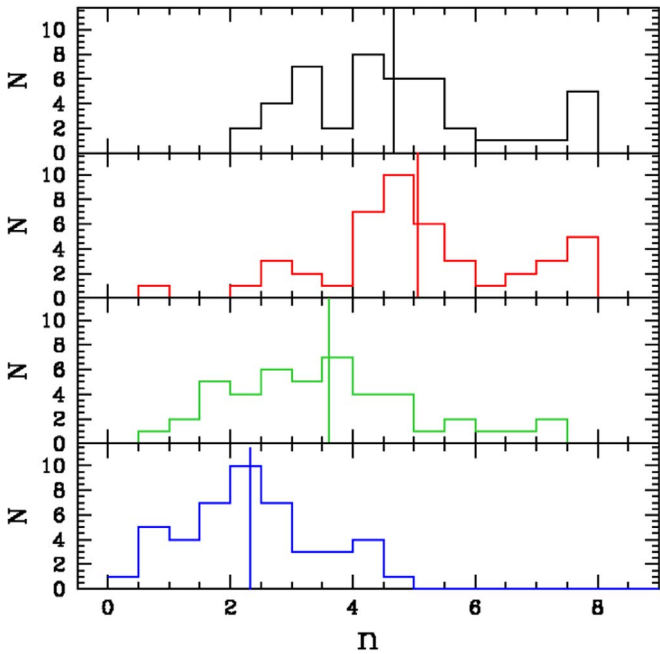


Figure 9. Histograms of the distributions of the Sérsic index n for the different classes of objects. The black histogram is for BCGs, the red for II-BCGs, the green for normal ETGs, and the blue for clusters. The solid lines mark the average values of the distributions.

simulations, including star, galaxy, and BH formation, tracking the expansion of the universe (Hinshaw et al. 2013).

We have used the run with full physics, including both BM and DM, having the highest degree of resolution, i.e., Illustris-1 (see Table 1 of Vogelsberger et al. 2014). A large number of different data are available for the subhalos inside this simulation. The former subhalos that we can call “simulated

galaxies” are those selected because the physics of the baryons inside them can be studied in straight comparison with the observational data. Among the many tabulated quantities provided for galaxies, we work in particular with the V -band photometry and the mass and half-mass radii of stellar particles (i.e., integrated stellar populations), for which Cartesian comoving coordinates (x' , y' , z') are available.

We have analyzed the projected light and mass profiles using the $z' = 0$ plane⁶ as a reference plane, and we have adopted the nonparametric morphology of Snyder et al. (2015). Starting from the V magnitudes and positions of the stellar particles, we have computed the effective radius R_e , the radial surface brightness profile in units of r/R_e , the best-fit Sérsic index, and the line-of-sight velocity dispersion.

The values of R_e are calculated considering only the star particles inside the friend-of-friends (FoFs) of galaxies and the galaxies inside the FoFs of clusters. We have set $z' = 0$ to project the coordinates of the stellar particles inside galaxies so that the velocity dispersion is calculated along the z' -axis.

Finally, we exploit the Cartesian coordinates of DM particles to characterize the average distribution of the surface mass density: in this case, we use the tabulated values of the half-mass radii to build up the radially normalized profiles of galaxies and clusters. As for the real galaxies, we have first normalized each profile to the effective radius and then calculated the average profiles of all classes of ETGs. The profiles have been built considering circular apertures in order to obtain the equivalent surface mass distribution. For these profiles, we have tested the Sérsic law as a fit of the projected mass distribution, providing the Sérsic parameters of the best

⁶ The choice of the projecting plane does not alter the conclusion drawn below.

fits for the single galaxies and clusters. The same fits have been applied to the average profiles.

To make the comparison with observations easier, we have built up the simulated data sets as follows. Starting from the 20 most massive clusters (halo masses in the range from 2.77×10^{13} to $2.55 \times 10^{14} h^{-1} M_{\odot}$) at redshift $z = 0$, we have added three additional samples related to the galaxies inside the clusters, namely, 20 BCGs, 20 II-BCGs, and a smaller set of normal ETGs. For these objects, we have derived the same data available from observations.

The adopted procedure is the following. First, we get the data for the subhalos inside each cluster having nonzero stellar mass, and having photometric data. At the end of this step, BCGs and II-BCGs can be trivially extracted as the first two luminous objects in each of the 20 catalogs. Note that the most and/or second-most luminous objects may not be the most and/or second-most massive objects.

For selecting the random ETGs, we have used the nonparametric morphologies.⁷ We use in particular two quantities: the Gini coefficient G , which measures the homogeneity of the light flux of a galaxy coming from different pixels ranging from zero (same flux from all pixels) to 1 (1 pixel contains the flux of the whole galaxy), and M_{20} , which measures the second-order spatial moment of the pixels contributing 20% of the total luminosity (Lotz et al. 2004). Starting from the 25 galaxies with available morphologies and mass below $10^{10} M_{\odot}$ present in the simulation box at $z = 0$ observed with Camera 0 (i.e., the projection with $z' = 0$ defined by Torrey et al. 2015), we have chosen the objects residing in the 20 most massive clusters with a morphology as close as possible to that of an ETG. This implies the following choice for the coefficients: $M_{20} < -2.00$ and $G > 0.55$. With this criterion, we get a sample of only five ETGs. This choice has been based on the visual inspection of Figure 2 of Snyder et al. (2015) that clearly shows a well-defined limit between ETGs and spirals at these values of the coefficients. In changing these limits, we risk biasing our sample with a population of disk galaxies.

The details of these subhalos and the host cluster identifiers, together with the values of M_{20} and G and the stellar masses, are reported in Table 5 in the Appendix.

In Figure 10, we can see the histogram of the stellar mass of galaxy clusters inside the WINGS (solid black line) and Illustris (dashed blue line) sample (at $z = 0$). The top panel plots the mass inside R_{200} , while the bottom panel plots that within $3R_{200}$. For the WINGS sample, the stellar mass has been computed for 31 over 46 clusters, i.e., for those having a proper estimation of the mass and a Sérsic model with index $0.5 < n < 8$. We get the stellar mass using a constant M/L ratio in the outermost regions of the clusters (see Cariddi et al. 2018). This ratio can be followed along the whole cluster profile because the stellar mass of the more massive galaxies is known from the analysis of their spectral energy distribution (Fritz et al. 2007, 2011).

For the Illustris sample, we summed up all stellar mass particles inside $r = 3R_{200}$. As can be seen from the figure, the observed clusters are more massive (at least by a factor of 10) than the simulated ones, both at $r = R_{200}$ and $r = 3R_{200}$, with the distribution of the simulated data being narrower than that for real clusters. Moreover, the stellar masses of the simulated

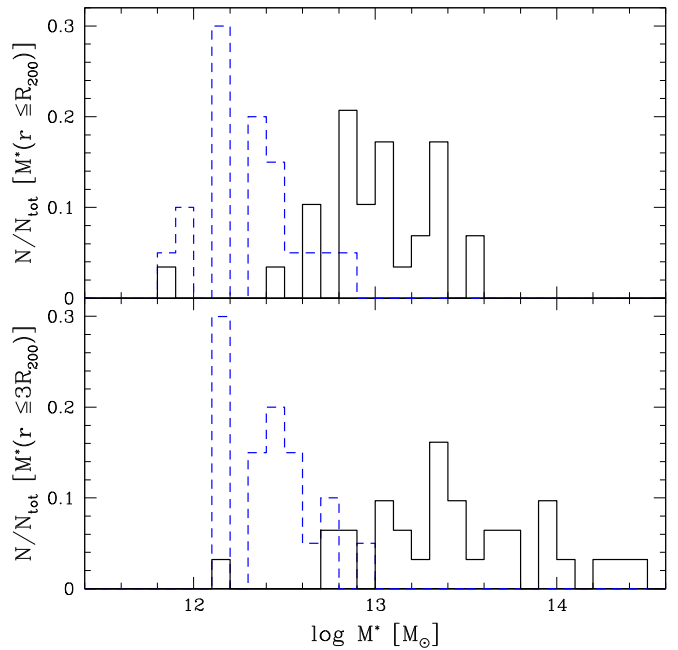


Figure 10. Histograms of the stellar mass distribution of real (black line) and simulated (blue line) clusters. The top panel shows the comparison of the mass enclosed within $r = R_{200}$, while the bottom panel shows that inside $r = 3R_{200}$.

clusters do not increase significantly while varying the enclosing radius; this may be due either to a higher-mass concentration of simulated clusters with respect to the real ones or to an overefficiency of the feedback effects on the star formation of galaxies (for a detailed overview of drawbacks in Illustris related to feedback, see, e.g., Genel et al. 2014; Vogelsberger et al. 2014; Sparre et al. 2015). This is the first discrepancy we observe between real and artificial data.

Figure 11 shows the absolute V magnitudes of real (top panel) and simulated (bottom panel) objects. Note again the large discrepancy between simulated and real clusters. Simulated BCGs appear a bit systematically brighter than real BCGs. The II-BCGs are a bit brighter too, while for normal ETGs, the statistics is poor (but note that the five objects we get are fainter than normal real ETGs).

In Figure 12, we see the comparison between the average profile of our BCGs and the equivalent average profile derived for simulated BCGs. The solid (dashed) line marks the observed (simulated) data. Once shifted in surface brightness for a constant value, the agreement is excellent, with the exception of only the inner region inside $0.5R_e$. Only a small part of this difference might be attributed to the seeing effect. One should, in fact, consider that the effective radius of BCGs is several times larger than the PSF. For the WINGS clusters, the FWHM of the seeing was around $1''$, and that at the typical distance of the clusters corresponds to about 1 kpc (a radius from 10 to ~ 100 times smaller than the typical R_e). This means that when we scale the profile in units of r/R_e , the region of influence of the PSF is always much lower than $0.1r/R_e$. The difference we see in the right panel of Figure 12 starts at $r/R_e = 0.5$ and reaches ~ 1 mag at $r/R_e = 0.1$. We therefore conclude that it could not be attributed to seeing. More likely, simulated data are still not very precise in the region of the SMBH (see, e.g., Vogelsberger et al. 2014 for a discussion in terms of stellar masses and the stellar mass function of galaxies).

⁷ These morphologies were derived for the g band, but this does not alter the comparison with the V -band data used here.

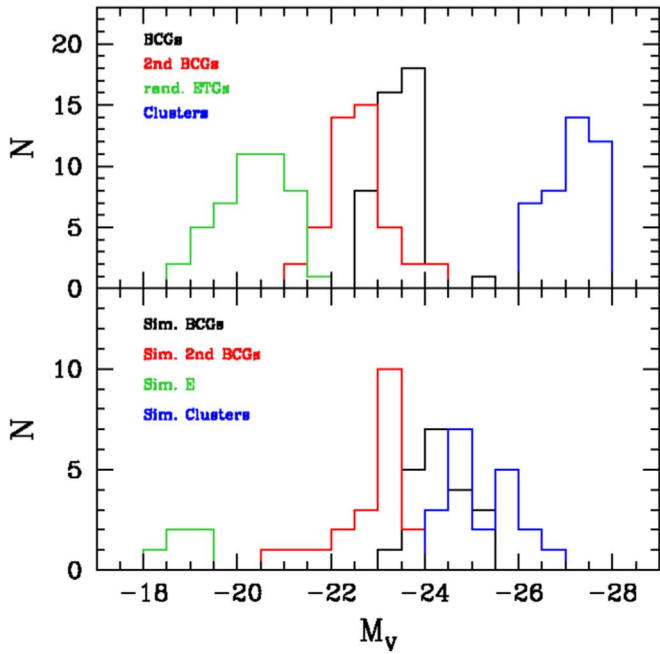


Figure 11. Histograms of the absolute V magnitudes of real (top panel) and simulated (bottom panel) objects.

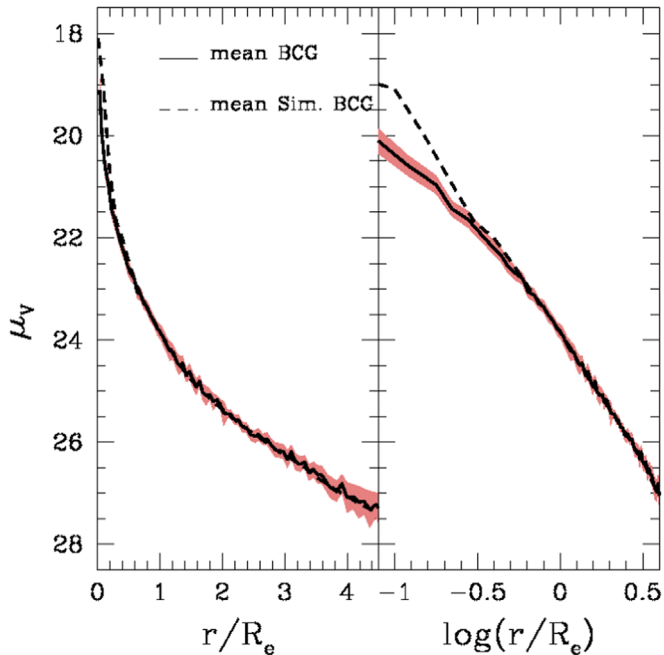


Figure 12. Comparison of the mean equivalent surface brightness profile of simulated BCGs (dotted line) with respect to real BCGs (solid line). The simulated profile has been artificially shifted in surface brightness to match the observed data. Left panel: r/R_e in linear scale. Right panel: r/R_e in log scale. The color band marks the 1σ standard deviation around the mean BCG profile.

In Figure 13, we present the average surface brightness profiles for all of our structures at $z = 0$ in log scale. The solid lines are used for the observed objects, keeping the same colors as previous figures for BCGs, II-BCGs, normal ETGs, and clusters. The dashed lines are used for simulated galaxies and clusters of the Illustris-1 data set. Each profile has been superposed to the simulated BCGs by imposing the vertical shift calculated by Equation (1). The values of the shifts are listed in Table 3.

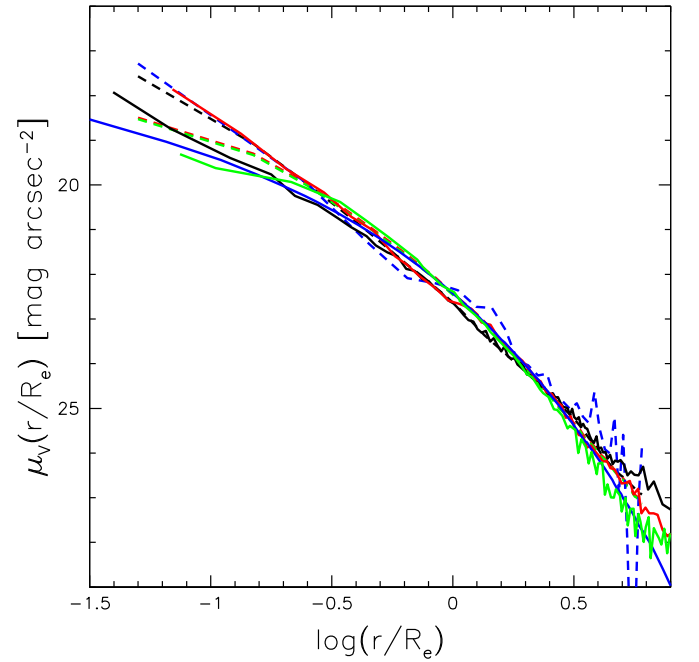


Figure 13. Average surface brightness profiles for observed (solid lines) and simulated (dashed lines) structures at $z = 0$. The BCGs are in black, II-BCGs in red, normal ETGs in green, and clusters in blue. The profiles have been vertically shifted by a constant value with respect to the BCG profile used as reference. See text.

Table 3
Values of the Constant Shift s_j Used to Superpose the Average Surface Brightness Profiles of Figure 13

Obs. Obj.	s_j
BCG	-1.2
II-BCG	-0.4
ETG	-1.3
CL	-7.8
Sim. obj.	s_j
II-BCG	1.9
ETG	0.9
CL	-3.3

Note. The average profile used as reference is that of our simulated BCGs.

Again, the superposition of the profiles at $r/R_e \in [0.3, 3.0]$ is remarkable, especially if we consider that the physical values of R_e span more than two decades. The log scale permits us to better see the differences in the inner region. We observe that the II-BCGs depart from the BCGs in both simulations and observations, although in two different fashions: the observed II-BCGs are, on average, more cuspy than the BCGs, at variance with simulations in which the opposite is true. In the left panel of Figure 5, we have shown the 1σ uncertainty around the mean profiles for the various classes of objects, so when we compare these two figures, we can say that the difference between real and simulated BCGs and II-BCGs is only marginally significant. However, the opposite trend seen in the inner regions in observations and simulations should be in some way related to the recipe adopted to follow the growth of the SMBHs and the AGN feedback.

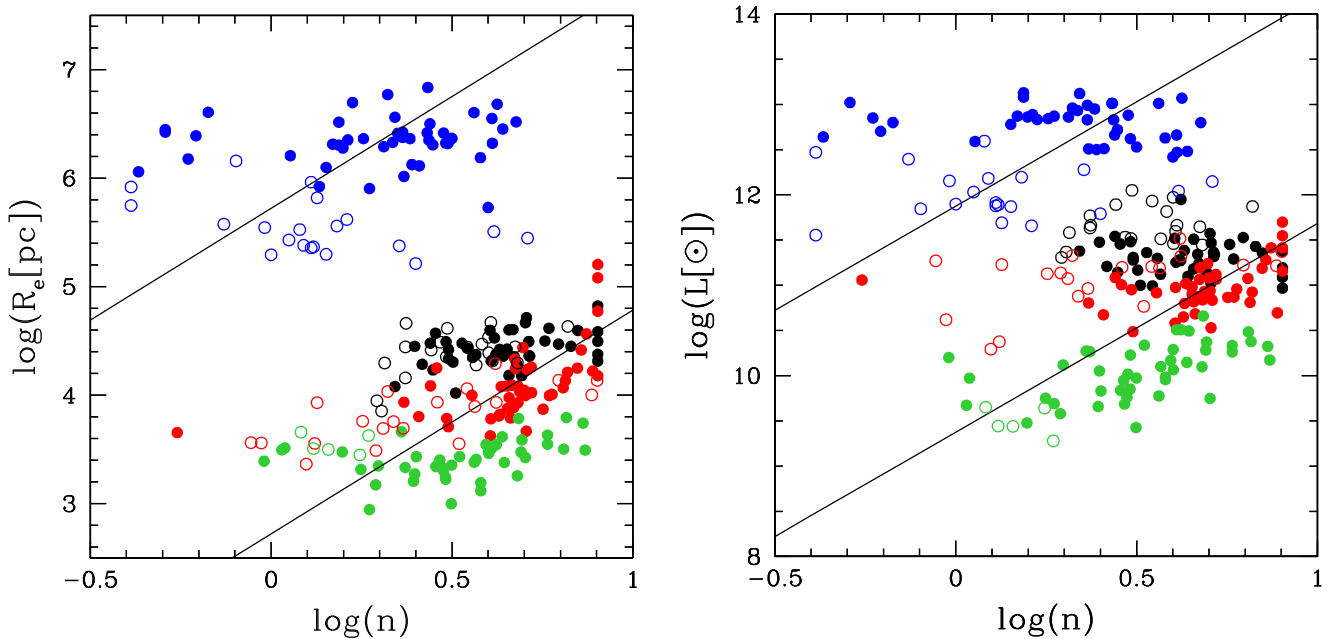


Figure 14. Left panel: distribution of ETGs and clusters in the $\log(R_e)$ – $\log(n)$ plane. Black dots are BCGs, red dots are II-BCGs, green dots are random ETGs, and blue dots are clusters. The simulated data have the same colors but are marked by open circles. The lower solid line marks the fit of the whole distribution of observed ETGs (BCGs+II-BCGs+random normal ETGs). The upper solid line is a shifted version of this fit used to best match the cluster distribution. Right panel: distribution of ETGs and clusters in the $\log(L)$ – $\log(n)$ plane. The symbols are the same as in the left panel. The lower solid line marks the fit of the whole distribution of observed ETGs (BCGs+II-BCGs+random normal ETGs). The upper solid line is a shifted version of the lower solid line done to best match the cluster distribution.

Looking at random ETGs (green lines), we can see that the simulated profile stands very close to real galaxies and clusters, although the simulated average profile is slightly more cored in the center.

Instead, clusters have significant differences. The average simulated cluster profile is much steeper in the center than that of real clusters, and in the outer parts, the profile is very noisy and seems a bit smoother than observed. Clearly, as noted above, simulations do not reproduce the cluster properties sufficiently well.

The nonperfect match of the light profiles of real and simulated objects is the second discrepancy between observations and simulations.

We now apply the Anderson–Darling criterion developed by Scholz & Stephens (1987) to test the hypothesis that the observed distributions in the 1D surface brightness light profiles $\mu_V(r)$ have a common origin. We make the two-sample test rather than the three-sample test that just gives an overall value. For the comparison between BCGs and normal ETGs, we get a p -value of 0.006, meaning a 0.6% chance that the two samples come from the same distribution. We can then reject the common distribution hypothesis safely. For the II-BCGs versus the normal ETGs, we get a p -value of 0.009, meaning a 0.9% chance, so we can also reject the common distribution hypothesis. For BCGs and II-BCGs, the p -value is 0.94, meaning a 94% chance that the two samples come from the same distribution. The common distribution hypothesis is thus supported.

The classical Kolmogorov–Smirnov test, which is differently sensitive in the tails of the distribution, gives a p -value of 0.003 for the comparison BCGs–normal ETGs, 0.006 for the comparison II-BCGs–normal ETGs, and 0.86 for the comparison BCGs–II-BCGs, confirming the substantial similarity of the mean profiles of BCGs and II-BCGs and discarding the hypothesis of a common origin of these objects with normal ETGs.

4.1. Nonhomology in Simulations

In order to check the nonhomology, we used the Sérsic law to fit the luminosity growth curves of the single profiles of BCGs, II-BCGs, normal galaxies, and clusters extracted from simulations. Figure 14 shows real (filled symbols) and simulated (open symbols) objects in the same diagrams as Figure 8. In both, we see that BCGs and II-BCGs show the same trend visible for real galaxies, even if there is a systematic difference in luminosity and radius (in particular, for clusters). The large interval in the values of n confirms that simulations are able to reproduce the observed spread of shapes of galaxies and clusters and therefore that, in general, the structures emerging from merging events are not self-similar.

The values of n measured for the average profiles of simulated galaxies are listed in Table 2. They are quite similar to those seen for real galaxies in the case of II-BCGs, but systematic variations are visible for the other classes. Taking into account how the final value of n depends on several factors, we can conclude that simulations successfully reproduce ETGs but fail with galaxy clusters.

4.2. The Progenitors of Simulated Galaxies

We have followed the SubLink merger trees of simulated galaxies (for details, see, e.g., Rodriguez-Gomez et al. 2015) to map the evolution of all of the subhalos back in time. We use the relevant data at redshift $z = 0, 0.2$ (i.e., at a look-back time $t_{\text{lb}} \sim 2.6$ Gyr), and 0.8 ($t_{\text{lb}} \sim 7.0$ Gyr). With these data, we show here the evolution of the effective radius and half-mass radius of BCGs and II-BCGs up to redshift $z = 0.8$.

The first thing we want to stress is that the progenitors of the present BCGs are also BCGs at that epoch (BCGs are known to be already in place at $z \sim 1$; see, e.g., De Lucia & Blaizot 2007), while the progenitors of the present II-BCGs are not necessarily the second-brightest objects in the clusters

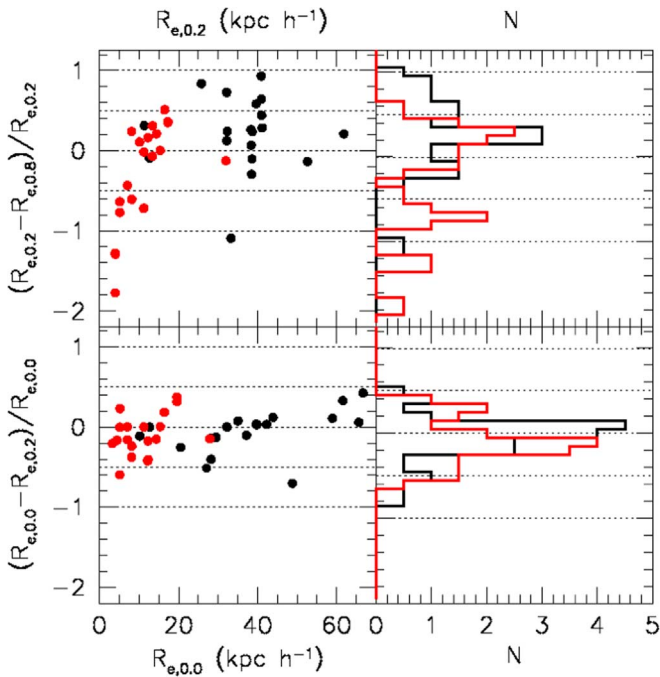


Figure 15. Evolution of R_e for BCGs and II-BCGs in the Illustris simulation, evaluated at three reference epochs (top panels: from $z = 0.8$ to 0.2 ; bottom panels: from $z = 0.2$ to 0.0). In the left panels, we display the final values of R_e against the differences (final–initial)/final; black circles represent BCGs, and red squares represent II-BCGs. In the right panels, the histograms show the overall behavior of the two data sets, with the black line representing BCGs and the red line representing II-BCGs. In both panels, the dotted lines mark the relative variation of R_e (0%, $\pm 50\%$, and $\pm 100\%$).

at the past considered epochs. The II-BCG observed at $z = 0$ is the final result of two competing effects: it is a galaxy that has experienced fast growth through merging, surviving as a II-BCG in the merger tree of the simulation, but at the same time, it is an object that lives in the innermost cluster region, where disruptive phenomena are at work. This peculiar evolution of the II-BCGs will be much clearer below when we look at the evolution of the effective radius of galaxies.

In Figure 15, we show the evolution of R_e through three reference epochs for the 20 main progenitor branches of BCGs and II-BCGs. We display for each BCG (black circles and histograms) and II-BCG (red squares and histograms) the variations of R_e normalized to the final values reached at $z = 0.2$ (top panel) and 0.0 (bottom panel). The dotted lines mark the percentage of variation (0%, $\pm 50\%$, and $\pm 100\%$).

We note that both positive and negative variations of R_e are present for BCGs and II-BCGs. This analysis aims at giving a profile-oriented insight on the average evolution of our objects. In the top panels of Figure 15, BCGs and II-BCGs show two broad distributions, having their maximum peak where the radius changes by $\sim +30\%$. Looking at BCGs, their effective radii most likely tend to increase, with growths of $\gtrsim 50\%$ in five cases over 20. The ample range of values of $\Delta R_e/R_e$ covered by BCGs passing from $z = 0.8$ to 0.2 sheds light on an important feature: although they can be considered as already assembled in terms of overall large mass and photometric output, structural properties like, e.g., the concentration of stellar light (and thus mass) are still evolving.

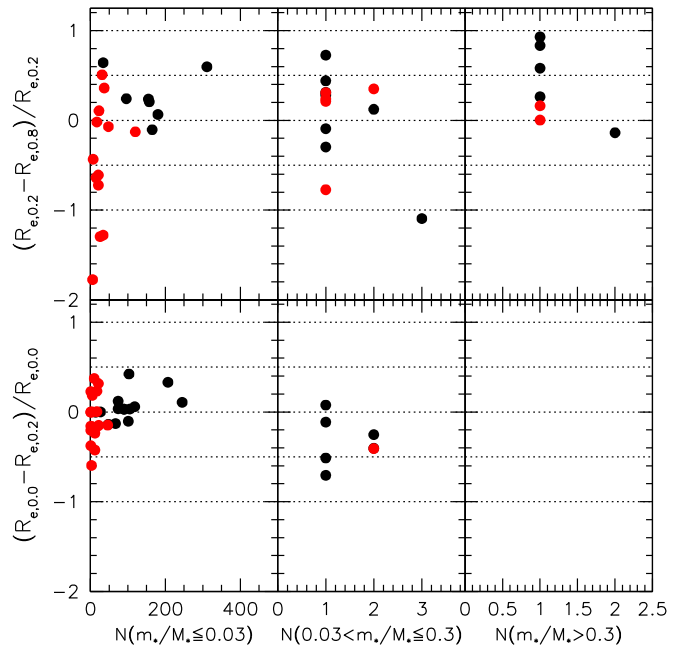


Figure 16. Relative variation of R_e vs. the number of merging events. Black dots mark BCGs, while red dots mark II-BCGs. From left to right, the mass ratio between the donor and main progenitor increases. The dotted lines mark the percentage of variation (0%, $\pm 50\%$, and $\pm 100\%$).

The II-BCGs have a more ample range of behaviors and also a number of minor peaks at negative values. In this context and with the chosen reference epochs, the high degree of complexity in the buildup of II-BCGs can be appreciated, being, as already stated, a particular subsample of galaxies evolving faster and more violently than others. In the bottom panel, the histograms related to BCGs and II-BCGs are quite similar in terms of both width and value of the peak: this suggests that II-BCGs in the last ~ 2.6 Gyr have evolved and consolidated into a more homogeneous sample.

With the Kolmogorov–Smirnov test, we have checked the hypothesis of evolution of the effective radius R_e from $z = 0.8$ to 0.2 and 0 . For the BCG sample, the comparison of R_e between $z = 0.8$ and 0.2 we get a probability of 0.008 , discarding the null hypothesis of an equal distribution of the radius at these epochs. On the other hand, the comparison of R_e between $z = 0.2$ and 0 gives a probability of 0.77 , which implies an almost equal distribution of R_e at these epochs. For the II-BCGs, the test gives a probability of 0.27 in the comparison of R_e between $z = 0.8$ and 0.2 and of 0.96 for the comparison of R_e between $z = 0.2$ and 0 . For these objects, the evolution of the effective radius is less marked, although again, the more marked variation occurs between $z = 0.8$ and 0.2 .

Finally, Figure 16 shows the same variations of R_e as a function of the number of merging events that BCGs and II-BCGs have experienced. In the left panel, we give the number of small merging events, expressed as the ratio of the mass m^* of the donor with respect to that of M^* of the main progenitor. In the right panels, we observe that the number of big merging events is null today.

In conclusion, we can say that both positive and negative variations of R_e are observed in the hierarchical simulations, but a net average variation of R_e is present from $z = 0.8$ and 0.2 . At closer epochs, the average radius of BCGs and II-BCGs does not change very much.

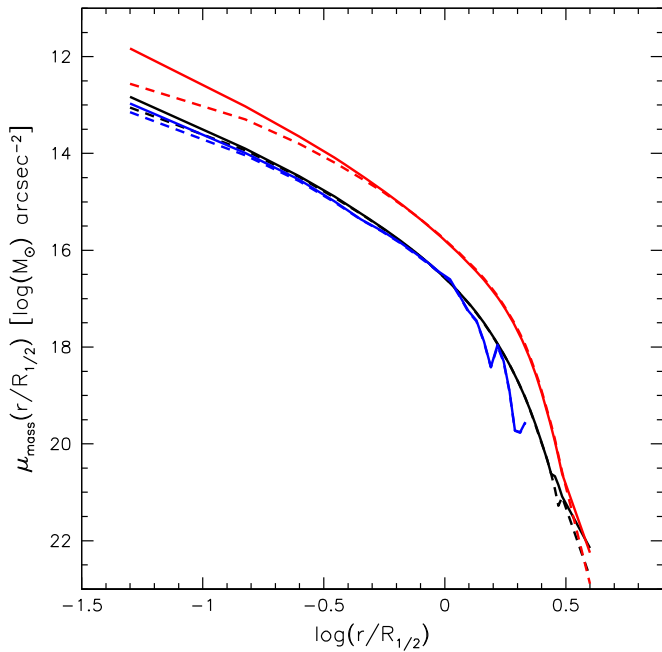


Figure 17. Average surface mass profiles μ_m for BCGs (black lines), II-BCGs (red lines), and clusters (blue lines) at $z = 0.0$ from simulations. Dashed lines refer to average profiles of DM only, while solid lines refer to DM+StM particles. No rescaling has been made in this plot.

4.3. Surface Mass Density Profiles

As already claimed by Merritt et al. (2005), the Sérsic law can give an equally optimum fit of the surface mass density profile as the NFW. In that paper, they noted that the energy distribution of the Sérsic law is roughly Boltzmann, and they argued that this is a maximum-entropy state resulting from mixing that occurred during violent relaxation or merger events (see also Binney 1982; Merritt et al. 1989; Ciotti 1991). Since the DM halos are also well mixed and approximated by a power law (Taylor & Navarro 2001), they suggested that the scale-free property of the Sérsic law is a feature in common between dark and luminous spheroids. In other words, the Sérsic law is a “universal profile” for all types of structures formed by merging.

In the following, we want to test whether the surface mass density profiles of our structures that emerged from simulations are indeed well fitted by the Sérsic law. We have therefore repeated the analysis done for the surface brightness profiles, looking now at the DM and DM+stellar matter (StM) distributions inside BCGs, II-BCGs, and clusters.

For the sake of clarity in this work, we use the following definition of surface mass density:

$$\mu_m(r) \equiv -2.5 \log \left(\frac{1}{2\pi r} \frac{dM}{dr} \right). \quad (3)$$

As for the surface brightness, this quantity grows toward positive values in the presence of less dense 2D regions. We evaluated $\mu_m(r)$ inside the circular annuli of a radius between r and $r + dr$ and, as we did for the photometric data, projected the mass onto the $z = 0$ plane.

We begin by presenting the average radial profiles at $z = 0$ in Figure 17. The dashed lines refer to DM-only profiles, while the solid lines are those of DM+StM. Black lines are used for

BCGs, red lines for II-BCGs, and blue lines for clusters. Here $R_{1/2}$ is determined by considering not only the matter distribution but also the relative abundance of each species. The main contributor is therefore DM, with stellar particles and other species (e.g., gas, BHs) contributing only marginally. For these reasons, $R_{1/2} > R_e$ for each structure, and consequently, the observed distributions have a much more important drop-off in density at relatively lower values of the normalized radial distance.

For clusters, in order to keep the BM into account, we have included the galaxies embedded in the DM subhalos.

At variance with Figure 13, no rescaling has been made in plotting the average profiles. One trivial consideration looking at Figure 17 is that the inclusion of stellar particles leads to steeper profiles, especially in the central regions, because more matter is included in the same radial bins. In general, the shapes of the profiles are quite similar, with II-BCGs standing above BCGs and clusters (see also Figure 4).

The first thing to stress is that now, the projected mass profiles are normalized to the half-mass radius $R_{1/2}$, which is related to all kinds of massive particles in the simulation.

The second important thing to note is that, at variance with light profiles, the surface mass density profiles begin to be very noisy for $r > 3 R_{1/2}$. This is also true for the average profiles. The reason is that the lower the $R_{1/2}$, the less mass present in the outskirts, and in turn, the greater the impact of mergers in shaping the outermost region of a profile. For this reason, our analysis is focused on the region $r \leq 3 R_{1/2}$.

Figure 18 shows the results of the fits obtained for the surface mass density of BCGs (left panel), II-BCGs (middle panel), and clusters (right panel). The average mass density is evaluated at $z = 0$.

We have separated the fits of the DM+StM profiles (green squares) from those of pure DM profiles (black, red, and blue circles) for BCGs, II-BCGs, and clusters, respectively). For clusters, we plot the average profile in the range $[0, 2 R_{1/2}]$.

An important thing to keep in mind is that adding galaxies inside clusters is not the same as adding stellar mass inside galaxies: the distribution of galaxies inside clusters could be very different in the outermost regions. It follows that often the DM+StM profiles can be quite different from the DM-only profiles, particularly in the outer radial bins.

This source of noise in clusters motivates us to fit the average profile of clusters only for $r < R_{1/2}$.

Figure 18 indicates that the projected mass distributions follow the Sérsic law quite well: the fits are well within the error bars. In Table 4, we list the values of the best fits obtained for the various classes of objects at different cosmic epochs.

Note that the values of n are quite different according to the selected intervals in radius for the fits. With the exception of clusters, the values of n are lower than 2 when $r/R_{1/2} \in [0, 3]$. We no longer see the progressive decrease of n visible in the fits of the luminous component in BCGs, II-BCGs, and clusters.

The rms deviation between the average profiles and their Sérsic fit was calculated as follows:

$$\begin{aligned} \sigma_m^2 &\equiv \langle \Delta \mu_m^2 \rangle \\ &= \frac{1}{N} \sum_{i=1}^N (\mu_m(r_i/R_{1/2}) - \mu_{m,\text{fit}}(r_i/R_{1/2}))^2. \end{aligned} \quad (4)$$

A direct comparison with the σ_m found by Merritt et al. (2005) is not easy because they fitted the Sérsic law on the

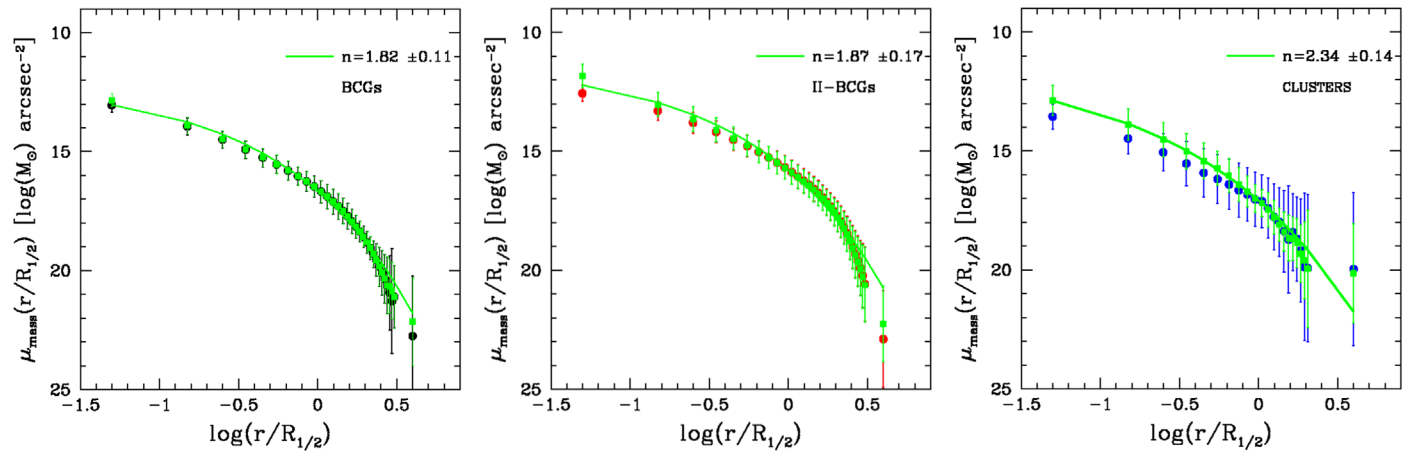


Figure 18. Sérsic fit for the average mass profiles of BCGs (left panel), II-BCGs (middle panel), and clusters (right panel). Error bars mark the 1σ rms of each radial bin. Green dots are used for the DM+StM matter, while black, red, and blue dots are used for the DM in BCGs, II-BCGs, and clusters, respectively. The Sérsic indexes listed in the boxes refer to the fit of the DM+StM component, shown by a green line.

DM-only mass profiles using a normalized radial coordinate $X = R/R_e$ (see their Equation (1)). In this work, the Sérsic fit is done for the DM+StM mass profiles, and the radial coordinate is normalized to the half-mass radius $R_{1/2}$.

As already seen for the surface brightness profiles, the radial extension of the Sérsic fit and the normalization parameter are crucial for determining the final value of n .

In Table 4, we also report the rms evaluated by Equation (4). The last two columns list the values of σ_m obtained by fitting the individual profiles in the ranges $r/R_{1/2} \in [0, 1]$ (subscript 1) and $r/R_{1/2} \in [0, 3]$ (subscript 3) and the average profiles ($\langle \rangle$) in the same ranges. Galaxies at all reference epochs show the minimum rms when fitted in the range $r/R_{1/2} \in [0, 3]$, while clusters are best fitted only in the range $r/R_{1/2} \in [0, 1]$, because at larger radii, the uncertainties are too large.

In the Appendix, we provide in Tables 6–12 the least-squares fit values of the single profiles for galaxies and clusters. From these tables, we derive the mean values of σ_m reported in the last column of Table 4. Note that the rms values of the single profiles are higher than those related to the average profiles and that the errors related to the Sérsic parameters are lower than 10%.

In order to see how the normalization radius evolves in the selected epochs, we replicate Figure 15 in Figure 19 using the half-mass radius instead of R_e . The relative variations of the half-mass radius, either considering the StM (left panels) or the DM+StM (right panels), are quite similar. Both positive and negative variations are visible, as in the case of R_e .

Again with the Kolmogorov–Smirnov test, we have checked the hypothesis of the evolution of the half-mass radius $R_{1/2}$ from $z = 0.8$ to 0.2 and 0. For the BCG sample considering only the contribution of the StM, for the comparison of $R_{1/2}$ between $z = 0.8$ and 0.2, we get a probability of 0.02, discarding the null hypothesis of an equal distribution of the radius at these epochs. On the other hand, the comparison of $R_{1/2}$ between $z = 0.2$ and 0 gives a probability of 0.96, which implies an almost equal distribution of $R_{1/2}$ at these epochs. When we consider the DM+StM, the values of the probability are 0.27 and 0.50, respectively, for the two redshift intervals, indicating a mild evolution of the half-mass radius. For the II-BCGs with StM only, the test gives a probability of 0.27 in the comparison of $R_{1/2}$ between $z = 0.8$ and 0.2 and 0.77 for the comparison of $R_{1/2}$ between $z = 0.2$ and 0. With DM+StM,

we instead get 0.06 for both time intervals. In this last case, the test seems to indicate a larger probability of variation of the half-mass radius.

When we look at the distribution of the total mass (right panel of Figure 19), we remember that the DM is now the chief contributor; still, very dispersed histograms are visible for the II-BCGs in both the top and bottom panels. This clearly indicates that the assembly in terms of overall mass is still occurring at the selected epochs. In other words, the II-BCGs are much younger objects than the BCGs, whose radius is almost not evolving.

In conclusion, we can say that the Sérsic law is valid for both the luminous and dark components of all types of structures (both galaxies and clusters). The values of n , however, depend very much on the choice of fitting interval and the normalization radius used. The values of n are quite similar for the mass profiles, in particular when the large interval in radius is considered, while they are different for the luminous components according to the stellar mass of the system.

The idea of a universal profile implies that all structures start from subhalos of similar shapes and then evolve differently for the activity of the baryon component. This last depends not only on the stars formed but also on the merging history and feedback effects that might be quite different from galaxy to galaxy.

5. Conclusions and Discussion

This paper is the first of a series dedicated to the analysis of the parallelism of properties shown by clusters and ETGs. In particular, we have analyzed the behavior of their luminosity and mass profiles. By exploiting the data of the WINGS and Omega-WINGS surveys, we have created the average equivalent luminosity profiles for different classes of objects—BCGs, II-BCGs, normal ETGs, and clusters—and we have checked the degree of nonhomology of such systems. Then, using the data of the Illustris simulation, we have tested the ability of current hydrodynamical models to reproduce the observational data. These data have also permitted the analysis of the surface mass profiles and a check of the effective radius of ETGs at higher redshifts.

In summary, these are our main conclusions.

1. The equivalent observed luminosity profiles in the V band of all classes of objects, once normalized to the effective

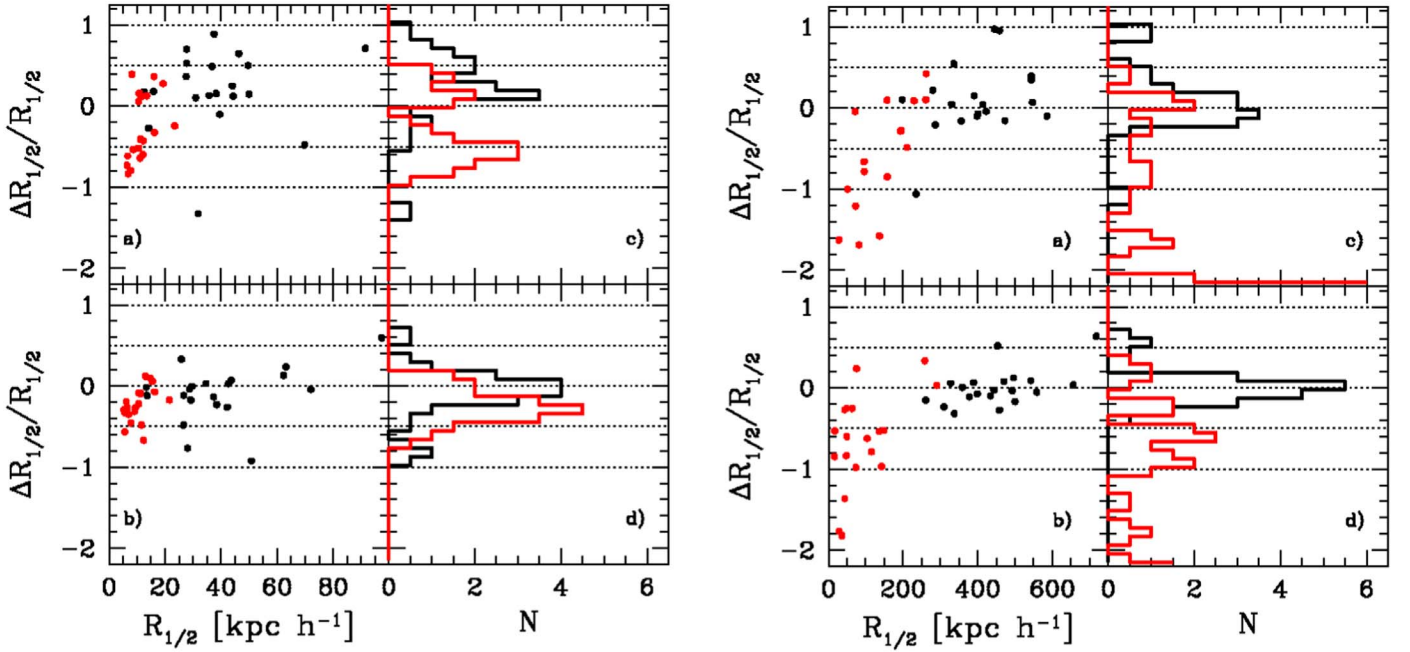


Figure 19. Left panel: Panel (a) shows the evolution of the half-mass radius considering only the contribution of the StM. The panel shows the relative variations of the half-mass radius evaluated at $z = 0.8$ and 0.2 . Black dots refer to BCGs and red dots to II-BCGs. Panel (b) shows the same variation for the redshift interval $z = 0.2$ to 0 . Panels (c) and (d) show the histograms of the relative half-mass variation at the selected epochs. The black line is used for BCGs and the red line for II-BCGs. Right panel: same as the left panel but using the half-mass radii obtained when the DM+StM matter inside galaxies is considered.

Table 4

Best Sérsic Parameters for the Average Surface Mass Density Profiles of Simulated BCGs, II-BCGs, and Clusters at the Three Selected Cosmic Epochs in the Ranges $r/R_{1/2} \in [0, 1]$ (Subscript 1) and $r/R_{1/2} \in [0, 3]$ (Subscript 3)

	n_1	Δn_1	$b_1(n)$	$\Delta b_1(n)$	n_3	Δn_3	$b_3(n)$	$\Delta b_3(n)$	$\sigma_{m(1,3)}$	$\langle \sigma_{m(1,3)} \rangle$
BCGs@ $z = 0$	3.87	0.17	6.30	0.18	1.82	0.11	4.15	0.22	0.01, 0.11	0.28, 0.25
BCGs@ $z = 0.2$	3.76	0.21	6.10	0.21	1.80	0.10	4.10	0.20	0.01, 0.11	0.24, 0.23
BCGs@ $z = 0.8$	3.86	0.24	6.10	0.25	1.33	0.08	3.28	0.22	0.02, 0.12	0.35, 0.31
II-BCGs@ $z = 0$	4.68	0.26	7.64	0.31	1.87	0.17	4.14	0.35	0.02, 0.24	0.34, 0.28
II-BCGs@ $z = 0.2$	6.28	0.16	9.52	0.19	1.70	0.16	3.94	0.34	0.02, 0.21	0.37, 0.29
II-BCGs@ $z = 0.8$	6.84	0.20	10.01	0.24	1.83	0.18	3.91	0.34	0.01, 0.22	0.33, 0.26
CLS@ $z = 0$	2.35	0.14	5.35	0.17	4.11	0.95	7.85	1.78	0.04, 0.45	0.52, 0.70

Note. The first three lines provide the fits for BCGs at $z = 0, 0.2,$ and $0.8,$ respectively. The second three lines give the same for II-BCGs. Clusters are fitted only at the present epoch. The errors Δn and Δb related to the parameters are given, as well as the values of the 1σ scatter obtained in the fits of the single and averaged profiles.

radius and shifted in surface brightness, can be superposed with a small scatter (≤ 0.3 mag).

2. The average profile of each class slightly deviates from the other, particularly in the inner and outer regions. The Anderson–Darling test does not support the hypothesis that BCGs and II-BCGs come from the same population of normal ETGs, while it does support the substantial similarity of the average profiles of BCG and II-BCGs. This means that, if ETGs start from a common universal profile, the subsequent evolution has almost completely changed the profile in the inner and outer regions, leaving the profile in the middle unaltered. We can then argue that all light profiles might originate from the same mass profile and later evolve for the numerous merging events and feedback effects of supernovae and AGNs. These events do not seem to have affected the bulk of the luminosity/mass distribution but have likely had a key role in determining the shift of the profiles of the big

galaxies with respect to that of normal ETGs. The presence of an SMBH in the center should have systematically changed the shape of the light profiles (Kormendy & Ho 2013). It is remarkable, although not fully statistically demonstrated, that the average II-BCG profile is steeper than that of BCGs in the center, while the opposite is true in the outer regions. We can only speculate on the reason for this at the moment. We believe that this behavior should be connected with the number of merging events (wet and dry) that a system has experienced during its evolution. The BCGs are at the center of the cluster potential, so they likely experienced several events of merging during their history. Some of them might have accreted SMBHs from other galaxies, increasing the total mass in the center. The presence of large masses in orbits around each other might have contributed to eliminating many stars from the central area (Bonfini & Graham 2016). This is the binary BH

scouring scenario. Another possibility has been suggested by Nipoti & Binney (2007), who argued that thermal evaporation of cold gas by virial-temperature gas might have played an important role in determining the shape of the inner profiles, since the analysis of the data reveals that galaxies with power-law profiles in the center have younger stellar populations than those with cores.

In the outer regions, on the other hand, the big number of dry mergers might have produced the observed extended stellar halos of BCGs and II-BCGs, with the first systems being much more frequently affected by these events.

Notably, galaxy clusters behave like normal ETGs and not like BCGs and II-BCGs. We argue that this is related to the merging history of clusters: as it occurs for low-luminosity ETGs, the number of dry merging events has not likely considerably altered the original light profile.

3. We have shown that the Sérsic law provides good fits of the luminous and dark components of galaxies and clusters and that all systems are nonhomologous, in the sense that their shapes cannot be predicted on the basis of their mass/luminosity.
4. The data of the Illustris simulation predict BCG and II-BCG light profiles quite similar to the observed ones. The effective radii and velocity dispersions are also quite similar to those observed, while clusters are still systematically less massive and luminous than real clusters at $z = 0$. The average light profiles of simulated galaxies can be well superposed to those of real galaxies, with small systematic deviations occurring only in the inner and outer regions. These differences likely originated from a still nonperfect receipt adopted for the merging and feedback effects. Simulated clusters have steeper profiles in the center than real clusters.
5. We have used the merger trees of BCGs and II-BCGs following their main progenitor branches to shed light on the evolution of their effective and half-mass radii with time; we have focused in particular on two reference past epochs, namely, $z = 0.2$ and 0.8 . It is evident that II-BCGs are still evolving at the selected epochs, while BCGs have seen only a moderate evolution. The progenitors of II-BCGs were not necessarily the II-BCGs of the clusters at these redshifts, while BCGs remain the brightest objects of the clusters. The effective radius can either be larger or smaller with respect to earlier epochs because of merging events.

From the comparison of R_e at different epochs, we argue the following. (i) Negative variations can be due to spontaneous dynamical cooling of the innermost regions, mergers having relatively massive star clumps and effectively reaching the innermost regions of the main progenitor, or a combination of both factors. Stripping events are also possible. (ii) Positive variations are likely due to the accretion of star clumps having nonnegligible mass and/or objects where infall is still occurring; here the amplitudes of the variations depend on the mass of the star clump compared to that of the central bulk, as well as on its radial position. Clearly, any combination of these

situations is possible; for example, massive galaxies most likely acquire smaller subhalos from the outskirts, so slight expansions of central volumes enclosing half the whole light (or mass) are expected. Moreover, because of the temporal separation between the three reference epochs, the galaxies of the samples might acquire large fractions of stars (or DM particles) immediately before $z = 0.2$ or 0 . This means that the galaxies are not fully relaxed.

6. Motivated by past theoretical studies devoted to the application of the Sérsic law to the distribution of matter, we have extended the analysis of simulated structures to the surface mass density profiles (μ_m , in terms of both average and single profiles). We find that the luminous matter plays a minimal role in shaping the profiles, and the DM gives the chief contributor. However, the average profiles are dominated by the former in the central regions of all structures, sensibly increasing the slopes of the profiles for $r/R_{1/2} \lesssim 0.3$. A significant departure from the self-similarity of the average profiles is evident over $r/R_{1/2} \sim 3$ for galaxies and $r/R_{1/2} \sim 1$ for clusters. Above these limits, constant minor mergers cause the structures to never reach relaxation in a Hubble time, while below these limits, the Sérsic law is able to fit the average profiles with very low rms. The profile analysis confirms that the luminous and dark components are strictly affecting each other.

In conclusion, galaxy clusters and ETGs show similar light and mass profiles that might come from the same original profile later evolved in different ways. The deviations forming this “seed” profile occur only in the inner and outer regions, where many physical effects are at work, in particular for the baryon component. All systems are nonhomologous, in the sense that their shapes, represented by the Sérsic index n , vary considerably within the same class of objects.

We kindly thank the anonymous referee for comments and suggestions that have greatly improved the paper. M.D. thanks Didier Fraix-Burnet for helpful discussions on the text of the paper. C.C. would like to thank the Department of Physics and Astronomy of Padua University for the hospitality and computational support.

Appendix

In this Appendix we report the stellar masses of five simulated ETGs and the results of the fits performed with the Sérsic law.

Table 5
Useful Physical Quantities of Five Random ETGs Extracted from the Illustris Data Set at $z = 0$ (See Text for More Details)

Subhalo ID	Cluster ID	M_{20}	G	M_* ($10^{10} M_\odot$)
000133	00	−1.99	0.60	0.438672
051847	03	−1.99	0.56	0.796838
080788	07	−1.99	0.56	0.580556
086214	08	−2.01	0.56	0.914614
120636	15	−1.99	0.57	0.692473

Table 6
Single Sérsic Parameters for Surface Mass Density Profiles of BCGs at $z = 0$

	$\mu_m(R_{1/2})$	n	Δn	$b(n)$	$\Delta b(n)$	$\sigma_m(\leq R_{1/2})$	$\sigma_m(\leq 3 R_{1/2})$
BCG@ $z = 0.0$,id:0	16.06	0.95	0.04	2.94	0.16	0.30	0.21
BCG@ $z = 0.0$,id:16937	15.76	0.53	0.04	1.06	0.17	0.64	0.45
BCG@ $z = 0.0$,id:30430	15.98	1.39	0.08	3.22	0.20	0.23	0.17
BCG@ $z = 0.0$,id:41088	16.51	2.61	0.11	5.33	0.21	0.03	0.08
BCG@ $z = 0.0$,id:51811	16.64	1.12	0.07	3.27	0.24	0.17	0.27
BCG@ $z = 0.0$,id:59384	16.21	1.50	0.12	3.49	0.30	0.21	0.24
BCG@ $z = 0.0$,id:66080	15.66	0.81	0.07	1.94	0.25	0.52	0.40
BCG@ $z = 0.0$,id:73663	17.74	4.03	0.66	8.17	1.26	0.19	0.23
BCG@ $z = 0.0$,id:80734	15.96	1.22	0.09	2.94	0.27	0.33	0.28
BCG@ $z = 0.0$,id:86186	16.30	1.68	0.07	3.72	0.17	0.15	0.12
BCG@ $z = 0.0$,id:93165	16.23	2.72	0.16	5.35	0.31	0.09	0.11
BCG@ $z = 0.0$,id:99148	16.61	2.20	0.13	4.73	0.28	0.13	0.13
BCG@ $z = 0.0$,id:104798	18.16	6.27	0.88	10.57	1.40	0.07	0.11
BCG@ $z = 0.0$,id:110567	17.03	2.53	0.14	5.35	0.28	0.14	0.11
BCG@ $z = 0.0$,id:114300	15.88	0.81	0.08	1.94	0.29	0.56	0.46
BCG@ $z = 0.0$,id:117343	15.95	1.44	0.11	3.10	0.27	0.26	0.23
BCG@ $z = 0.0$,id:120615	16.61	1.73	0.07	3.70	0.17	0.12	0.11
BCG@ $z = 0.0$,id:123773	15.82	0.29	0.04	0.24	0.11	0.88	0.94
BCG@ $z = 0.0$,id:127228	15.90	1.15	0.07	2.67	0.21	0.34	0.23
BCG@ $z = 0.0$,id:129770	16.62	1.64	0.08	3.74	0.20	0.17	0.14

Table 7
Single Sérsic Parameters for Surface Mass Density Profiles of BCGs at $z = 0.2$

	$\mu_m(R_{1/2})$	n	Δn	$b(n)$	$\Delta b(n)$	$\sigma_m(\leq R_{1/2})$	$\sigma_m(\leq 3 R_{1/2})$
BCG@ $z = 0.2$,id:0	16.40	1.57	0.08	3.96	0.23	0.11	0.17
BCG@ $z = 0.2$,id:11777	15.39	0.80	0.05	1.90	0.19	0.47	0.31
BCG@ $z = 0.2$,id:24088	16.17	1.29	0.07	3.01	0.18	0.20	0.17
BCG@ $z = 0.2$,id:33383	16.43	0.94	0.06	2.63	0.25	0.39	0.34
BCG@ $z = 0.2$,id:40441	17.60	2.42	0.10	5.42	0.23	0.05	0.09
BCG@ $z = 0.2$,id:46753	15.96	0.97	0.08	2.24	0.25	0.43	0.33
BCG@ $z = 0.2$,id:52457	16.16	1.44	0.10	3.26	0.24	0.21	0.20
BCG@ $z = 0.2$,id:57650	17.26	1.63	0.20	3.62	0.47	0.35	0.33
BCG@ $z = 0.2$,id:63467	16.22	2.02	0.09	4.20	0.20	0.06	0.11
BCG@ $z = 0.2$,id:68485	16.68	1.74	0.08	4.32	0.22	0.12	0.15
BCG@ $z = 0.2$,id:74066	15.98	1.02	0.06	2.48	0.20	0.37	0.25
BCG@ $z = 0.2$,id:78783	16.45	1.66	0.13	3.84	0.32	0.14	0.22
BCG@ $z = 0.2$,id:82944	17.71	5.47	1.37	10.80	2.56	0.11	0.26
BCG@ $z = 0.2$,id:86310	16.92	2.42	0.16	4.76	0.31	0.13	0.13
BCG@ $z = 0.2$,id:90381	16.44	1.36	0.13	2.95	0.32	0.32	0.29
BCG@ $z = 0.2$,id:93818	16.30	0.82	0.06	1.85	0.21	0.41	0.33
BCG@ $z = 0.2$,id:97243	16.34	1.31	0.09	2.85	0.24	0.24	0.22
BCG@ $z = 0.2$,id:100284	16.34	1.47	0.10	3.36	0.25	0.23	0.21
BCG@ $z = 0.2$,id:103005	16.76	1.33	0.08	3.27	0.23	0.19	0.21
BCG@ $z = 0.2$,id:132611	16.42	1.38	0.09	3.03	0.22	0.23	0.20

Table 8
Single Sérsic Parameters for Surface Mass Density Profiles of BCGs at $z = 0.8$

	$\mu_m(R_{1/2})$	n	Δn	$b(n)$	$\Delta b(n)$	$\sigma_m(\leq R_{1/2})$	$\sigma_m(\leq 3 R_{1/2})$
BCG@ $z = 0.8$,id:0	16.83	1.05	0.09	2.92	0.33	0.31	0.40
BCG@ $z = 0.8$,id:5951	16.09	0.57	0.07	1.26	0.29	0.68	0.71
BCG@ $z = 0.8$,id:10747	17.00	1.41	0.10	3.33	0.26	0.29	0.22
BCG@ $z = 0.8$,id:14807	12.33	1.35	0.10	2.96	0.24	0.16	0.22
BCG@ $z = 0.8$,id:18160	17.03	1.32	0.07	3.26	0.20	0.25	0.19
BCG@ $z = 0.8$,id:20984	16.97	1.05	0.08	2.49	0.26	0.34	0.32
BCG@ $z = 0.8$,id:23233	17.23	1.50	0.09	3.89	0.26	0.26	0.21
BCG@ $z = 0.8$,id:25993	16.63	1.43	0.11	3.13	0.28	0.23	0.23
BCG@ $z = 0.8$,id:28932	16.48	0.85	0.06	2.08	0.23	0.44	0.35
BCG@ $z = 0.8$,id:32025	16.62	0.74	0.06	1.76	0.24	0.48	0.42
BCG@ $z = 0.8$,id:34434	16.80	1.44	0.11	3.21	0.29	0.26	0.24
BCG@ $z = 0.8$,id:38876	16.93	1.29	0.09	2.83	0.24	0.27	0.23
BCG@ $z = 0.8$,id:40495	16.54	1.28	0.06	2.92	0.15	0.20	0.15
BCG@ $z = 0.8$,id:42332	13.58	0.50	0.05	1.00	0.23	0.71	0.61
BCG@ $z = 0.8$,id:44152	17.30	0.83	0.05	2.36	0.22	0.39	0.34
BCG@ $z = 0.8$,id:45976	16.68	1.44	0.09	3.23	0.24	0.28	0.20
BCG@ $z = 0.8$,id:60183	17.51	1.31	0.09	3.44	0.29	0.31	0.27
BCG@ $z = 0.8$,id:64890	16.77	1.39	0.14	3.31	0.38	0.36	0.33
BCG@ $z = 0.8$,id:108426	17.22	1.31	0.09	3.29	0.28	0.36	0.26
BCG@ $z = 0.8$,id:134538	17.04	0.99	0.07	2.34	0.23	0.43	0.29

Table 9
Single Sérsic Parameters for Surface Mass Density Profiles of II-BCGs at $z = 0$

	$\mu_m(R_{1/2})$	n	Δn	$b(n)$	$\Delta b(n)$	$\sigma_m(\leq R_{1/2})$	$\sigma_m(\leq 3 R_{1/2})$
SBCG@ $z = 0.0$,id:1	16.40	0.59	0.07	1.30	0.28	0.84	0.66
SBCG@ $z = 0.0$,id:16938	14.81	1.23	0.08	2.96	0.23	0.32	0.23
SBCG@ $z = 0.0$,id:30433	16.01	3.20	0.29	6.66	0.58	0.16	0.15
SBCG@ $z = 0.0$,id:41092	14.88	1.90	0.19	4.08	0.43	0.23	0.25
SBCG@ $z = 0.0$,id:51814	14.81	0.87	0.10	2.04	0.35	0.61	0.52
SBCG@ $z = 0.0$,id:59386	14.91	1.34	0.19	3.16	0.51	0.43	0.46
SBCG@ $z = 0.0$,id:66082	15.10	1.59	0.14	3.84	0.36	0.35	0.27
SBCG@ $z = 0.0$,id:73664	15.36	2.00	0.10	3.99	0.21	0.14	0.12
SBCG@ $z = 0.0$,id:80735	15.41	1.11	0.08	2.56	0.24	0.31	0.27
SBCG@ $z = 0.0$,id:86187	15.25	1.35	0.11	3.06	0.28	0.31	0.26
SBCG@ $z = 0.0$,id:93166	16.76	3.10	0.19	6.42	0.37	0.14	0.10
SBCG@ $z = 0.0$,id:99149	14.61	0.69	0.06	1.67	0.27	0.72	0.51
SBCG@ $z = 0.0$,id:104799	15.33	0.93	0.09	2.19	0.30	0.54	0.42
SBCG@ $z = 0.0$,id:110566	16.57	1.84	0.08	4.11	0.19	0.15	0.12
SBCG@ $z = 0.0$,id:114301	15.33	1.52	0.15	3.43	0.37	0.31	0.29
SBCG@ $z = 0.0$,id:117346	15.30	2.37	0.11	4.84	0.23	0.14	0.10
SBCG@ $z = 0.0$,id:120623	15.80	1.12	0.08	2.79	0.25	0.37	0.28
SBCG@ $z = 0.0$,id:123774	14.68	1.57	0.14	3.60	0.36	0.30	0.27
SBCG@ $z = 0.0$,id:127230	14.80	1.93	0.13	3.99	0.28	0.16	0.16
SBCG@ $z = 0.0$,id:129771	16.32	1.39	0.09	3.34	0.26	0.32	0.23

Table 10
Single Sérsic Parameters for Surface Mass Density Profiles of II-BCGs at $z = 0.2$

	$\mu_m(R_{1/2})$	n	Δn	$b(n)$	$\Delta b(n)$	$\sigma_m(\leq R_{1/2})$	$\sigma_m(\leq 3 R_{1/2})$
SBCG@ $z = 0.2$,id:11779	15.75	1.21	0.10	2.71	0.27	0.40	0.28
SBCG@ $z = 0.2$,id:24092	16.01	1.46	0.20	3.40	0.52	0.48	0.42
SBCG@ $z = 0.2$,id:33384	16.11	1.02	0.07	3.10	0.28	0.39	0.35
SBCG@ $z = 0.2$,id:40442	15.95	1.93	0.12	3.91	0.26	0.15	0.15
SBCG@ $z = 0.2$,id:46754	15.50	2.07	0.20	4.56	0.44	0.22	0.23
SBCG@ $z = 0.2$,id:57652	15.58	1.22	0.12	2.86	0.33	0.39	0.34
SBCG@ $z = 0.2$,id:68486	15.00	0.74	0.07	1.77	0.29	0.71	0.51
SBCG@ $z = 0.2$,id:74067	14.39	0.51	0.04	1.07	0.18	0.80	0.53
SBCG@ $z = 0.2$,id:82945	16.00	1.14	0.09	2.69	0.27	0.42	0.30
SBCG@ $z = 0.2$,id:86309	16.44	1.17	0.09	2.91	0.29	0.42	0.31
SBCG@ $z = 0.2$,id:90385	15.89	2.01	0.15	4.36	0.34	0.16	0.18
SBCG@ $z = 0.2$,id:97247	15.84	2.69	0.17	5.49	0.33	0.17	0.12
SBCG@ $z = 0.2$,id:100285	15.80	1.34	0.12	3.00	0.32	0.33	0.29
SBCG@ $z = 0.2$,id:103006	15.69	1.38	0.11	3.40	0.31	0.35	0.27
SBCG@ $z = 0.2$,id:105632	16.67	1.55	0.14	3.28	0.32	0.28	0.24
SBCG@ $z = 0.2$,id:137480	17.10	1.13	0.06	3.21	0.23	0.37	0.25
SBCG@ $z = 0.2$,id:176645	17.06	0.92	0.07	2.55	0.27	0.49	0.38
SBCG@ $z = 0.2$,id:180271	16.81	1.77	0.12	3.96	0.28	0.24	0.18
SBCG@ $z = 0.2$,id:230239	16.89	1.18	0.11	2.95	0.34	0.45	0.36
SBCG@ $z = 0.2$,id:358004	17.47	2.18	0.15	4.73	0.33	0.17	0.16

Table 11
Single Sérsic Parameters for Surface Mass Density Profiles of II-BCGs at $z = 0.8$

	$\mu_m(R_{1/2})$	n	Δn	$b(n)$	$\Delta b(n)$	$\sigma_m(\leq R_{1/2})$	$\sigma_m(\leq 3 R_{1/2})$
SBCG@ $z = 0.8$,id:36780	16.71	2.08	0.13	4.20	0.27	0.12	0.14
SBCG@ $z = 0.8$,id:53591	17.20	1.05	0.10	2.44	0.30	0.52	0.36
SBCG@ $z = 0.8$,id:72814	16.90	1.01	0.09	2.39	0.29	0.53	0.37
SBCG@ $z = 0.8$,id:75685	16.99	1.40	0.08	3.16	0.20	0.28	0.17
SBCG@ $z = 0.8$,id:83154	16.92	0.88	0.05	2.40	0.19	0.41	0.28
SBCG@ $z = 0.8$,id:88212	16.82	0.93	0.09	2.24	0.30	0.57	0.42
SBCG@ $z = 0.8$,id:92482	16.60	0.65	0.05	1.43	0.20	0.57	0.41
SBCG@ $z = 0.8$,id:101263	17.32	2.19	0.24	4.43	0.49	0.24	0.24
SBCG@ $z = 0.8$,id:106868	17.74	1.82	0.15	3.84	0.33	0.26	0.20
SBCG@ $z = 0.8$,id:114022	17.15	1.45	0.10	3.61	0.27	0.32	0.22
SBCG@ $z = 0.8$,id:118576	16.45	0.96	0.09	2.46	0.33	0.54	0.43
SBCG@ $z = 0.8$,id:125781	17.07	1.93	0.11	4.25	0.26	0.17	0.15
SBCG@ $z = 0.8$,id:128161	17.35	1.39	0.13	3.13	0.34	0.34	0.30
SBCG@ $z = 0.8$,id:171082	17.38	1.77	0.18	3.98	0.42	0.33	0.27
SBCG@ $z = 0.8$,id:174742	17.42	1.89	0.14	4.24	0.32	0.19	0.19
SBCG@ $z = 0.8$,id:175715	17.24	1.41	0.15	3.34	0.39	0.41	0.34
SBCG@ $z = 0.8$,id:202961	17.70	1.96	0.14	4.22	0.31	0.19	0.18
SBCG@ $z = 0.8$,id:213485	18.30	2.71	0.26	5.37	0.50	0.17	0.17
SBCG@ $z = 0.8$,id:236478	17.25	2.38	0.11	4.85	0.21	0.11	0.09
SBCG@ $z = 0.8$,id:281354	17.54	1.39	0.13	2.97	0.32	0.26	0.28

Table 12
Single Sérsic Parameters for Surface Mass Density Profiles of Clusters at $z = 0$

	$\mu_m(R_{1/2})$	n	Δn	$b(n)$	$\Delta b(n)$	$\sigma_m(\leq R_{1/2})$	$\sigma_m(\leq 3 R_{1/2})$
CL@z = 0.0.id:0	17.63	0.79	0.17	3.61	0.85	0.48	0.97
CL@z = 0.0.id:1	15.77	0.38	0.05	0.78	0.27	0.67	0.95
CL@z = 0.0.id:2	16.27	0.59	0.10	1.75	0.52	0.63	1.01
CL@z = 0.0.id:3	17.51	0.20	0.06	0.32	0.28	1.34	1.37
CL@z = 0.0.id:4	14.01	4.33	0.85	3.87	0.72	0.09	0.11
CL@z = 0.0.id:5	16.84	3.17	1.17	6.56	2.32	0.24	0.62
CL@z = 0.0.id:6	16.28	0.40	0.05	1.51	0.33	0.79	0.72
CL@z = 0.0.id:7	19.16	11.22	14.97	17.99	23.06	0.35	0.61
CL@z = 0.0.id:8	15.90	3.58	0.89	5.86	1.39	0.08	0.31
CL@z = 0.0.id:9	16.12	0.22	0.04	0.16	0.12	1.10	1.39
CL@z = 0.0.id:10	14.83	3.15	0.26	4.47	0.35	0.07	0.10
CL@z = 0.0.id:11	16.63	0.30	0.05	0.65	0.29	1.11	1.27
CL@z = 0.0.id:12	17.49	0.15	0.03	0.47	0.25	0.95	0.77
CL@z = 0.0.id:13	17.89	15.15	48.15	19.85	61.10	0.25	0.90
CL@z = 0.0.id:14	15.63	1.35	0.15	2.61	0.33	0.33	0.29
CL@z = 0.0.id:15	16.45	0.52	0.07	1.47	0.40	0.80	0.94
CL@z = 0.0.id:16	15.61	2.05	0.23	3.18	0.36	0.14	0.19
CL@z = 0.0.id:17	14.69
CL@z = 0.0.id:18	15.94	1.34	0.12	2.90	0.30	0.28	0.28
CL@z = 0.0.id:19	18.13	18.53	36.96	30.59	59.40	0.23	0.59

ORCID iDs

Mauro D'Onofrio  <https://orcid.org/0000-0001-6441-9044>

Mauro Sciaratta  <https://orcid.org/0000-0002-0962-5272>

Stefano Cariddi  <https://orcid.org/0000-0002-0364-7171>

Paola Marziani  <https://orcid.org/0000-0002-6058-4912>

Cesare Chiosi  <https://orcid.org/0000-0001-7107-8196>

References

- Abadi, M. G., Navarro, J. F., Fardal, M., Babul, A., & Steinmetz, M. 2010, *MNRAS*, 407, 435
- Adami, C., Mazure, A., Biviano, A., et al. 1998, *A&A*, 331, 493
- Barmby, P., McLaughlin, D. E., Harris, W. E., Harris, G. L. H., & Forbes, D. A. 2007, *AJ*, 133, 2764
- Binney, J. J. 1982, *MNRAS*, 200, 951
- Blumenthal, G. R., Faber, S. M., Flores, R., & Primack, J. R. 1986, *ApJ*, 301, 27
- Bonatto, C., & Bica, E. 2005, *A&A*, 437, 483
- Bonfini, P., & Graham, A. W. 2016, *ApJ*, 829, 81
- Caon, N., Capaccioli, M., & D'Onofrio, M. 1993, *MNRAS*, 265, 1013
- Cariddi, S., D'Onofrio, M., Fasano, G., et al. 2018, *A&A*, 609, 133
- Cava, A., Bettoni, D., & Poggianti, B. M. 2009, *A&A*, 495, 707
- Ciotti, L. 1991, *A&A*, 249, 99
- Ciotti, L., & Bertin, G. 1999, *A&A*, 352, 447
- De Lucia, G., & Blaizot, J. 2007, *MNRAS*, 375, 2
- Del Popolo, A., & Cardone, V. F. 2012, *MNRAS*, 423, 1060
- D'Onofrio, M., Bettoni, D., Bindoni, D., et al. 2011, *AN*, 334, 373
- D'Onofrio, M., Bindoni, D., Fasano, G., et al. 2014, *A&A*, 572, 87
- D'Onofrio, M., Capaccioli, M., & Caon, N. 1994, *MNRAS*, 271, 523
- Diehl, S., & Statler, T. S. 2005, *ApJL*, 633, L21
- Djorgovski, S. 1995, *ApJL*, 438, L29
- Djorgovski, S., & Davis, M. 1987, *ApJ*, 313, 59
- Dressler, A., Lynden-Bell, D., Burstein, D., et al. 1987, *ApJ*, 313, 42
- Dubinski, J., & Carlberg, R. G. 1991, *ApJ*, 378, 496
- Eliche-Moral, M. C., Balcells, M., Aguerri, J. A. L., & Gonzalez-Garcia, A. C. 2006, *A&A*, 457, 91
- El-Zant, A., Shlosman, I., & Hoffman, Y. 2001, *ApJ*, 560, 636
- Faber, S. M., & Jackson, R. E. 1976, *ApJ*, 204, 668
- Fasano, G., Bettoni, D., Ascaso, B., et al. 2010, *MNRAS*, 404, 1490
- Fasano, G., Marmo, C., Varela, J., et al. 2006, *A&A*, 445, 805
- Feigelson, E. D., & Babu, G. J. 1992, *ApJ*, 397, 55
- Fritz, J., Poggianti, B. M., Bettoni, D., et al. 2007, *A&A*, 470, 137
- Fritz, J., Poggianti, B. M., Cava, A., et al. 2011, *A&A*, 526, A45
- Genel, S., Vogelsberger, M., Springel, V., et al. 2014, *MNRAS*, 445, 175
- Ghigna, S., Moore, B., Governato, F., et al. 2000, *ApJ*, 544, 616
- Gnedin, O. Y., Kravtsov, A. V., Klypin, A. A., & Nagai, D. 2004, *ApJ*, 616, 16
- Governato, F., Brook, C., Mayer, L., et al. 2010, *Natur*, 463, 203
- Governato, F., Zolotov, A., Pontzen, A., et al. 2012, *MNRAS*, 422, 1231
- Graham, A., & Colless, M. 1997, in *ASP Conf. 116*, ed. M. Arnaboldi et al. (San Francisco, CA: ASP), 175
- Graham, A. W. 2001, *AJ*, 121, 820
- Graham, A. W. 2002, *ApJL*, 568, L13
- Graham, A. W. 2004, *ApJ*, 613L, 33
- Graham, A. W., Erwin, P., Trujillo, I., & Ramos, A. A. 2003, *AJ*, 125, 2951
- Graham, A. W., & Guzmán, R. 2003, *AJ*, 125, 2936
- Gullieuszik, M., Poggianti, B. M., Fasano, G., et al. 2015, *A&A*, 581, 41
- Hamilton, T. S., Casertano, S., & Turnshek, D. A. 2006, *NewAR*, 50, 758
- Hinshaw, G., Larson, D., Komatsu, E., et al. 2013, *ApJS*, 208, 19
- Hopkins, P. F., Hernquist, L., Cox, T. J., Robertson, B., & Krause, E. 2007, *ApJ*, 669, 67
- Kormendy, J. 1977, *ApJ*, 218, 333
- Kormendy, J., & Ho, L. C. 2013, *ARA&A*, 51, 511
- Lanzoni, B., Ciotti, L., Cappi, A., Tormen, G., & Zamorani, G. 2004, *ApJ*, 600, 640
- Lotz, J. M., Primack, J., & Madau, P. 2004, *AJ*, 128, 163
- Martizzi, D., Teyssier, R., & Moore, B. 2012, *MNRAS*, 420, 2859
- McLaughlin, D. E. 2000, *ApJ*, 539, 618
- Menci, N., Rosati, P., Gobat, R., et al. 2008, *ApJ*, 685, 863
- Merritt, D., Graham, A. W., Moore, B., Diemand, J., & Terzić, B. 2006, *AJ*, 132, 2685
- Merritt, D., Navarro, J. F., Ludlow, A., & Jenkins, A. 2005, *ApJ*, 624, 85
- Merritt, D., Piatek, S., Portegies Zwart, S., & Hemsendorf, M. 2004, *ApJL*, 608, L25
- Merritt, D., Tremaine, S., & Johnstone, D. 1989, *MNRAS*, 236, 829
- Milosavljevic, M., Merritt, D., Rest, A., & van den Bosch, F. C. 2002, *MNRAS*, 331, L51
- Moore, B., Governato, F., Quinn, T., Stadel, J., & Lake, G. 1998, *ApJL*, 499, L5
- Moretti, A., Gullieuszik, M., Poggianti, B. M., et al. 2014a, *A&A*, 599, 81
- Moretti, A., Poggianti, B. M., Fasano, G., et al. 2014b, *A&A*, 564, 138
- Navarro, J. F., Frenk, C. S., & White, S. D. M. 1996, *ApJ*, 462, 563
- Navarro, J. F., Ludlow, A., Springel, V., et al. 2010, *MNRAS*, 402, 21
- Nelson, D., Pillepich, A., Genel, S., et al. 2015, *A&C*, 13, 12
- Nipoti, C., & Binney, J. 2007, *MNRAS*, 382, 1481
- Nipoti, C., Treu, T., Ciotti, L., & Stiavelli, M. 2004, *MNRAS*, 355, 1119
- Pedrosa, S., Tissera, P. B., & Scannapieco, C. 2009, *MNRAS*, 395, L57
- Peirani, S., Kay, S., & Silk, J. 2008, *A&A*, 479, 123

- Pignatelli, E., Fasano, G., & Cassata, P. 2006, *A&A*, 446, 373
- Preto, M., Merritt, D., & Spurzem, R. 2004, *ApJL*, 613, L109
- Ravindranath, S., Ho, L. C., & Filippenko, A. V. 2002, *ApJ*, 566, 801
- Rodriguez-Gomez, V., Genel, S., Vogelsberger, M., et al. 2015, *MNRAS*, 449, 49
- Romano-Díaz, E., Shlosman, I., Hoffman, Y., & Heller, C. 2008, *ApJL*, 685, L105
- Scannapieco, C., & Tissera, P. B. 2003, *MNRAS*, 338, 880
- Schaeffer, R., Maurogordato, S., Cappi, A., & Bernardeu, F. 1993, *MNRAS*, 263, L21
- Scholz, F. W., & Stephens, M. A. 1987, *J. Am. Stat. Assoc.*, 82, 918
- Sérsic, J. L. 1968, Atlas de Galaxies Australes (Córdoba: Obs. Astron., Univ. Nac. Córdoba)
- Snyder, G. F., Torrey, P., Lotz, J. M., et al. 2015, *MNRAS*, 454, 1886
- Sparre, M., Hayward, C. C., Springel, V., et al. 2015, *MNRAS*, 447, 3548
- Taylor, J. E., & Navarro, J. F. 2001, *ApJ*, 563, 483
- Torrey, P., Snyder, G. F., Vogelsberger, M., et al. 2015, *MNRAS*, 447, 2753
- Trujillo, I., Erwin, P., Ramos, A. A., & Graham, A. W. 2004, *AJ*, 127, 1917
- Varela, J., D'Onofrio, M., Marmo, C., et al. 2009, *A&A*, 497, 667
- van der Marel, R. 1999, *AJ*, 117, 744
- Vogelsberger, M., Genel, S., Springel, V., et al. 2014, *Natur*, 509, 177
- Zaritsky, D., Gonzalez, A. H., & Zabludoff, A. I. 2006, *ApJ*, 638, 725